Experimental investigation of cross flow mixing in a randomly packed bed and streamwise vortex characteristics using particle image velocimetry and proper orthogonal decomposition analysis

T. Nguyen,[1, a)] R. Muyshondt,[2, b)] Y. Hassan,[1, c)] and N.K. Anand[2, d)]

[1)]*Department of Nuclear Engineering, Texas A& M University*

[2)]*Department of Mechanical Engineering, Texas A& M University*

Study of flow and heat transfer through porous media or randomly packed beds is important as these configurations are widely used in many engineering applications, for example heat energy storage, chemical catalytic reactors, and nuclear reactors. The flow mixing characteristics in a cross-flow plane of a facility with randomly packed spheres at an aspect ratio of 6.3 were experimentally investigated. The velocity fields at several regions of the cross-flow plane located in the vicinity of the wall and in the pores between spheres were obtained by applying the matched-index-of-refraction and time-resolved particle image velocimetry (TR-PIV) techniques for Reynolds numbers ranging from 700 to 1,700. The TR-PIV results revealed various flow patterns in the transverse plane of the packed spheres, including swirling flow structures aligned with the axial flow direction, a strong bypass flow near the enclosure wall, and a circulation region created when the bypass flow ejected into a large spatial gap. When the Reynolds number was increased, the peaks of root-mean-square fluctuating velocities, u'_{rms} and v'_{rms}, were found to increase approximately at the same ratio as the increase in Reynolds number, and the magnitude of the Reynolds stress increased considerably. In addition, the characteristics of flow mixing in different flow regions were investigated via the two-point cross-correlation of fluctuating velocities. Using Taylor's hypothesis, the vorticity iso-surfaces were constructed. Thus constructed iso-surfaces showed that shear layers generated from the bypass flow gaps were stretched, broken into smaller flow structures, and then evolved as vortex pairs when entering the neighboring gaps. The results obtained by applying proper orthogonal decomposition (POD) analysis to the velocity fields showed that the statistically dominant flow structures had approximately the same size and shape as those depicted by Taylor's hypothesis. Vortex characteristics, such as populations, spatial distributions, and strengths, for various spatial regions and Reynolds numbers were obtained by a combination of POD analysis and vortex identification.

[a)]Electronic mail: thien.duy.ng@tamu.edu

[b)]Electronic mail: muyshondt@tamu.edu

[c)]Electronic mail: y-hassan@tamu.edu

[d)]Electronic mail: nkanand@tamu.edu

This manuscript was accepted by Phys. Fluids. Click here to see the version of record.

Nomenclature

$\langle . \rangle$	time-averaged operator
ω	vorticity (s^{-1})
ε_N	absolute difference between the statistics
η	separation length (mm)
$\mu_\Gamma, \sigma_\Gamma$	mean and standard deviation of vortex strength (mm^2/s)
μ_A, σ_A	mean and standard deviation of vortex area (mm^2)
μ_{pcy}	dynamic viscosity of p-cymene (Pa×s)
ν_{pcy}	kinematic viscosity of p-cymene (m^2/s)
Ω_z	vorticity in z-direction
ρ_{pcy}	density of p-cymene (kg/m^3)
τ	time delay (s)
R_{uu0}, R_{vv0}	velocity-velocity spatial cross-correlation coefficients
R_{uu}, R_{vv}	velocity-velocity spatial-temporal cross-correlation coefficients
Re	Reynolds number
ε_b	porosity
D	bed diameter (mm)
d_h	effective hydraulic diameter (mm)
d_p	sphere diameter (mm)
f	sampling frequency (Hz)
L_x, L_y	integral length scales (mm)
N	number of samples
N_Ω	counts of detected vortices
U, V	time-averaged velocities (m/s) along x and y directions
u', v'	fluctuating velocities (m/s) along x and y directions
U_m	interstitial velocity (m/s)
U_g	superficial velocity (m/s)
x, y	x and y flow directions in the transverse plane

I. Introduction

Proper understanding of the physics of fluids inside random porous media or randomly packed beds is very important because they are widely used in many diverse engineering applications[1]. These include heat storage systems, cooling and/or heating of granular materials[2], chemical catalytic reactors for processing and distillation, ground water contamination and remediation[3], water infiltration in soil[4], contamination plumes[5], oil recovery[6–9], magnetic refrigerators, fuel cells[10], nutrient transport through mammalian tissues[11], and nuclear reactors. Other engineering applications of flow in porous media can be reviewed in the works of[12],[13],[7], and[14].

Flows in porous media and randomly packed beds exhibit a wide spectrum of complex flow structures continuously evolving in space and time[15], and play an important role in the natural and engineered processes mentioned above. The complexity of flows in randomly packed beds

arises from the complex geometries and randomly connected void spaces within randomly packed beds, i.e., the structures of heterogeneous media[13,16], have hindered efforts to characterize the underlying transport phenomena occurring within them.

This paper discusses experimental studies on a facility of randomly packed spheres that could represent a chemical reactor and/or a reactor core of an advanced high temperature nuclear reactors (AHTR). Chemical catalysts, consisting of pellets or beads, are commonly used in the synthesis of basic chemicals and intermediates at large scales using gaseous reactants. The AHTR concept leverages a particle-based fuel format consisting of discrete spherical graphite pebbles arrayed in a packed bed architecture. Thermal regulation is achieved via the flow of gas (e.g., helium) or liquid (e.g., molten salt) coolants through the void spaces between the pebbles in the bed, with the characteristic pebble diameters being 6 cm for gas-cooled reactors, and 3 cm for liquid-cooled reactors. In the above mentioned engineering applications, a critical design challenge involves understanding the complex flow field, heat and mass transfer phenomena occurring within the interstitial regions between the packing materials. For instance, in packed beds with pebble diameters ranging from 6 mm to 30 mm, i.e., the size ranges that are most commonly found in the engineering applications mentioned above[4,8–10,15,17], there are various pore sizes ranging from a few millimeters to less than 1 mm[7,13–15]. Confining wall effects and inhomogeneous porosity within the bed make flow mixing and thermal transfers within the void spaces very complicated. Various flows regimes, i.e. from laminar to turbulent or vice versa, may occur within the gaps; heat and mass transfers in packed bed systems may be locally enhanced and/or reduced. Hot spots and thermal fatigue have been observed on the surfaces of several packed spheres due to the poor transport of flow and heat transfer at those locations. The predominant approach to model transports in packed beds has been adopting a porous media viewpoint to construct a lumped-parameter representation of the bed, from which the bulk characteristics of the flow can be obtained. Although this approach is useful for estimating the global scale effects, it inherently neglects details associated with the complex localized flow fields within individual pores. The macroscopic processes that direct material transport in porous media are manifestations of the interplay between flow behaviors spanning an incredibly broad range of length scales from macroscopic to individual pore levels. Dispersion, for example, emerges as a consequence of the cumulative effects of microscale phenomena, including mixing caused by solid obstructions in the flow path, incomplete connectivity of the medium, eddies in the medium, and recirculation caused by local pressure gradients. Based upon volume averages of microscale parameters, the macroscopic picture obscures the underlying transport phenomena, making it difficult to rationally develop physics-based simulation tools capable of accurately capturing behavior across a broad spectrum of conditions.

Pressure drops across the axial length of packed beds and dispersions are macroscopic parameters that have been discussed in numerous studies, such as those of[18],[19],[20],[21],[22], and[23]. Fully leveraging the advantages of flows in randomly packed spheres requires a fundamental understanding of the complex flow characteristics within packed bed systems. Recent improvements in computer capabilities have made numerical simulations and computational fluid dynamics (CFD) valuable tools to study flow characteristics, flow mixing, and transport properties at pore scales for

flows in porous media. However, due to the complexity of three-dimensional (3D) flow geometries and randomly connected pores within randomly packed beds, most numerical simulations of flow transports at the pore scale are based on different versions of Reynolds-Averaged Navier-Stokes (RANS) approaches[24]. For instance, the RANS simulations of[25] and[26] consisted of the temporal-volume averaging process of the extended Darcy-Forchheimer model equations. On the other hand,[27] and[28] employed macroscopic turbulence models based on volume averaging the RANS equations. Recently, there have been several numerical studies of randomly packed beds at the pore scales such as the direct numerical simulation (DNS) of[29], the high-resolution simulations of a single face or multiple cubic centered pebble bed using large-eddy simulations (LES) of[30], and the quasi-DNS of[31,32], and[33–35].

Because of the complex geometries of packed bed systems, experimental measurements to obtain the flow characteristics in porous media and/or randomly packed beds are commonly based on a combination of the matching-refractive-index approach and laser-based techniques. For examples, readers can review the previous experimental studies of[36],[37], and[38] for their laser-Doppler anemometry (LDA) measurements (single-point measurement technique); the two-dimensional two-component (2D2C) planar particle tracking velocimetry (PTV) velocity measurements in packed beds of[39],[40],[41], and[42]; the 2D2C particle image velocimetry (PIV) measurements in the studies of[43],[44],[45],[46–48],[49], and[50]; and the two-dimensional three-component (2D3C) stereoscopic PIV measurements of[51] and[52]. It is known that complex geometries of packed beds have presented challenges to experimental, numerical and theoretical researchers for constructing advanced transport models, which were previously based on volume averages of micro-scale parameters, to improve the models' predictive capabilities. Full-field experimental measurements at high spatial and temporal resolutions are essential to perform the mapping of complex flow patterns in packed bed systems and the volume-averaging of flow parameters for better and more accurate flow predictions.

The focus of the present study is to investigate the flow mixing characteristics in a cross flow plane of a facility of randomly packed spheres at an aspect ratio of 6.3 and Reynolds numbers of $Re_1 = 700$, $Re_2 = 1{,}200$, and $Re_3 = 1{,}700$. The considered Reynolds numbers covered a range of flow conditions from turbulent transition to fully turbulent flow for packed beds[46–49]. Velocity measurements were performed on a transverse plane by combining the approaches of the matched-index-of-refraction (MIR) and time-resolved particle image velocimetry (TR-PIV) techniques. This combined approach allows us to non-invasively measure the flow fields in the transverse plane located near the wall and in the pores between spheres with high spatial and temporal resolutions. The obtained experimental results will provide insight into the flow characteristics of flow mixing in packed bed systems, and of bypass flows in high-temperature pebble bed reactors (HTR-PBRs). In the context of this study, bypass flow refers to flow between the enclosure wall and spheres. Spatial gaps between the spheres and the wall normally have a wider distribution and larger sizes[53] compared to those between the spheres located within the central regions of packed beds. Therefore, bypass flows created within the near-wall regions have unique characteristics, such as accelerated and/or decelerated flows when passing smaller and/or larger spatial gaps, or a

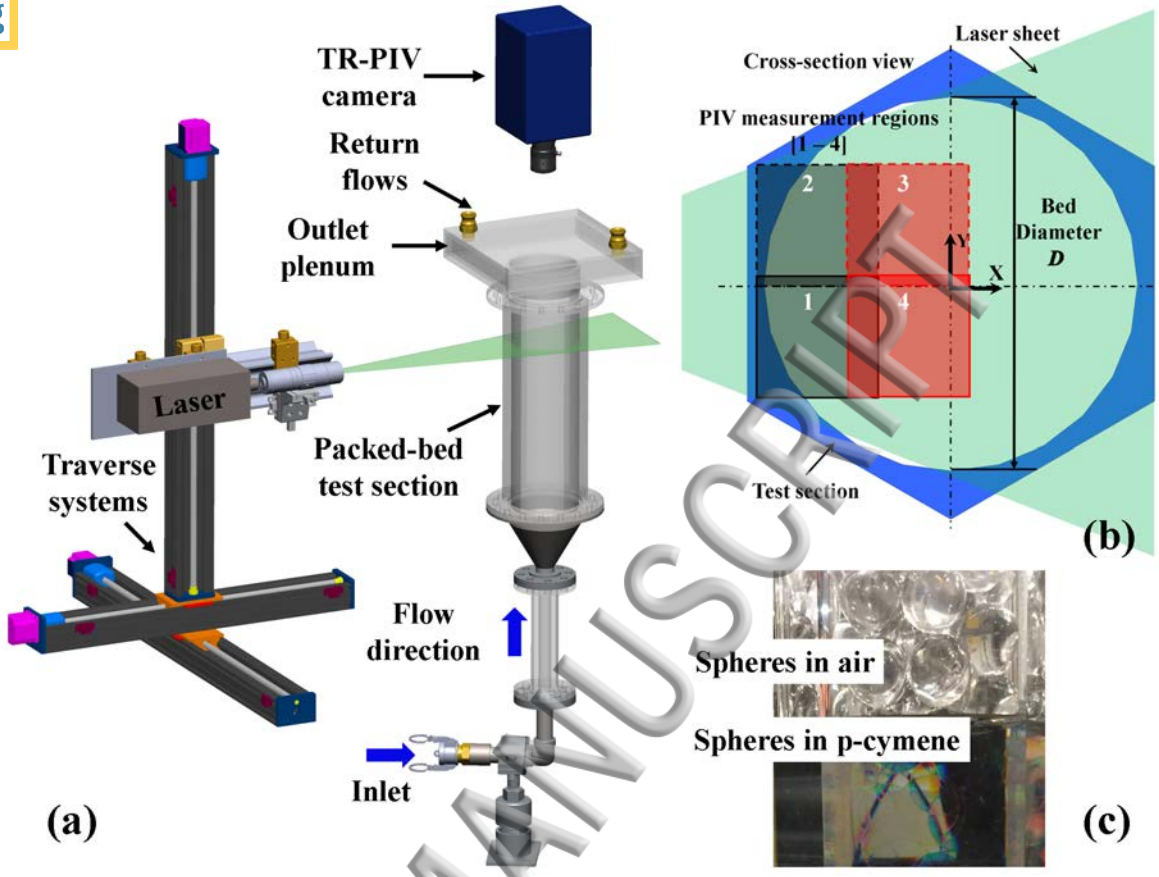

FIG. 1. Overview of the MIR experimental facility of randomly packed spheres and the TR-PIV experimental setup. *(a)* Flow loop with the TR-PIV measurement setup, *(b)* top view of the test section showing the TR-PIV measurement areas, and *(c)* MIR test section of the packed spheres partially filled with p-cymene.

large circulation flow region within the flow gap. These features of bypass flow have been considered an important issue related to the flow and heat transfer capabilities, and efficiency of not only pebble bed reactors[19], but also of other advanced reactor designs, such as prismatic reactors[54–56].

The rest of this paper is structured as follows. The MIR experimental facility of randomly packed spheres and the TR-PIV experimental setup for velocity measurements on the transverse plane are presented in Section II. The statistical results computed from the TR-PIV measurements are discussed in Section III, while the visualization of vortical structures using Taylor's hypothesis is presented in Section III C. An analysis of the two-point velocity cross-correlation is discussed in Section IV, and the velocity decomposition using proper orthogonal decomposition (POD) analysis to extract the statistically dominant flow structures is presented in Section V. In Section VI, we describe vortex characteristics, such as populations, spatial distributions, and strengths, by applying the POD analysis and vortex identification.

This manuscript was accepted by Phys. Fluids. Click here to see the version of record.

II. Experimental facility and TR-PIV experimental setup

A. Matched-index-of-refraction experimental facility of randomly packed spheres

This section describes the experimental facility of randomly packed spheres, featuring the MIR approach for velocity measurements in the cross-flow plane. An overview of the MIR experimental facility, which includes a flow loop and a test section is shown in Figure 1(a). The flow loop consisted of a 100-liter storage tank, a primary centrifugal pump connected to a variable frequency drive to control the flow rates, a Coriolis flow meter, and a transparent test section of randomly packed spheres. The fluid flow from the tank was driven by the pump to enter the inlet pipe and the test section, exit, and return to the tank. The test section, which had a total axial length of 457.2 mm, had a hexagonal enclosure and a circular interior cross-section with a diameter of 139.7 mm. The test section and the spheres were made of transparent poly-methyl methacrylate (acrylic), which had the same refractive index ($n = 1.49$) of the operating fluid, named p-cymene, at room temperature (20^{o}C). The p-cymene had a density, ρ_{pcy}, of 855 kg·m^{-3}, and a dynamic viscosity, μ_{pcy}, of $8.1 \cdot 10^{-4}$ Pa·s[57]. Figure 1(c) shows the principle idea of the MIR approach that we applied to build the experimental facility of randomly packed spheres. In this figure, when the test section was partially filled with p-cymene, the spheres at the bottom part of the test section became invisible in the fluid region. This allows the use non-intrusive, laser-based, optical measurement techniques, such as the PIV technique in the present study, to quantify the displacement of fluid elements[58]. A number of researchers have successfully used p-cymene as the fluid for their MIR experimental facilities which allows for non-intrusive velocity measurements via laser-based techniques, i.e. LDV and PIV techniques, such as using a column of dispersed beads[38], packed beds of spheres[42,45], and bundles of rods[59–61].

In the current study, we used spheres with a diameter of $d_p = 22.2$ mm, yielding a bed-to-bead ratio of $D/d_p = 6.3$, and a porosity of $\varepsilon_b = 0.395$. For flows in packed beds, the effective hydraulic diameter, d_h, is estimated by

$$d_h = d_p \frac{\varepsilon_b}{1 - \varepsilon_b}, \tag{1}$$

and the modified Reynolds number is defined by

$$Re = \rho_{pcy} U_m d_h / \mu_{pcy}, \tag{2}$$

where μ_{pcy} is the dynamic viscosity of the operating fluid and, U_m is the interstitial velocity, which is the characteristic velocity within the spatial gaps between the spheres. The averaged bed velocity U_g (or U_{Darcy} velocity) is calculated by $U_g = Q/A_{bed}$, where Q is the volumetric flow rate and A_{bed} is the total cross-sectional area of the bed. The interstitial velocity U_m can be estimated from the averaged bed velocity by $U_m = U_g/\varepsilon_b$. Flow measurements were performed along the cross-plane of the test section. Details of the TR-PIV experimental setup and velocity measurements are presented in the next section.

This manuscript was accepted by Phys. Fluids. Click here to see the version of record.

B. TR-PIV experimental setup

Figure 1(a) illustrates the experimental setup for the TR-PIV measurements in the facility of randomly packed spheres, whereas Figure 1(b) shows a cross-section (xy-plane) of the test section and the TR-PIV measurement areas. The TR-PIV system consisted of a 20 W continuous green laser (wavelength $\lambda = 532$ nm) and a Phantom Fastcam SA5 camera with a full 12-bit depth image resolution of $1{,}024 \times 1{,}024$ pixels. The laser was mounted on linear traverses, and the laser beam was adjusted by using a combined laser optics system to illuminate a 2-mm-thick horizontal plane perpendicular to the flow direction. The camera was equipped with a Nikkor 200 mm lens, which orthogonally viewed the horizontal xy-plane, and was positioned on three-axis motorized linear translation stages. The seeding particles were hollow glass spheres with a mean diameter of 10 μm and a density of 1.6 g/cm^3 that were pre-mixed in the storage tank and circulated through the entire flow loop. Therefore, the seeding particles were entirely mixed and present throughout the test section of packed beds. Such highly reflective seeding particles were illuminated by the laser sheet, and the reflected light from particles was captured by the camera to create an image. A sequence of images was then captured and analyzed using PIV cross-correlation algorithms to obtain the particles' displacements.

In the TR-PIV measurements made in the transverse plane, four measurement regions, denoted as Regions 1, 2, 3, and 4, illuminated by the laser sheet as shown in Figure 1(b). The transverse plane had an altitude of 838.2 mm from the inlet pipe or 419.1 mm from the entrance of the test section. The origin of the coordinate system was established at the center of the circular cross-section, where the x and y coordinates represent in-transverse plane directions. In this study, velocity measurements were performed at Reynolds numbers of Re_1, Re_2, and Re_3. The camera operated at speeds of 1,000, 1,500, and 2,000 frames-per-second (fps) for velocity measurements at Reynolds numbers Re_1, Re_2, and Re_3, respectively. We followed the suggestions of[62] and[58] to identify the camera operating frame rates that yielded small enough time-intervals between two successive images and resulted in out-of-plane particle displacements less than one tenth of the laser thickness.

TABLE I. Estimated uncertainties, e_{Re_1}, e_{Re_2}, and e_{Re_3}, for the statistical results obtained from the TR-PIV measurements on Regions 1, 2, 3 and 4 at Reynolds numbers Re_1, Re_2, and Re_3, respectively. The values shown here are maximal and normalized by the interstitial velocity U_m.

	U/U_m (%)			V/U_m (%)			u'_{rms}/U_m (%)			v'_{rms}/U_m (%)			$u'v'/U_m^2$ (%)		
	e_{Re_1}	e_{Re_2}	e_{Re_3}	e_{Re_1}	e_{Re_2}	e_{Re_3}	e_{Re_1}	e_{Re_1}	e_{Re_3}	e_{Re_1}	e_{Re_2}	e_{Re_3}	e_{Re_1}	e_{Re_2}	e_{Re_3}
Region 1	0.58	0.82	1.35	0.65	0.79	1.33	0.41	0.58	0.96	0.46	0.56	0.94	0.39	0.43	0.63
Region 2	0.66	0.79	1.35	0.63	0.76	1.34	0.47	0.56	0.96	0.45	0.54	0.95	0.25	0.27	0.49
Region 3	0.52	0.74	1.27	0.69	0.85	1.38	0.37	0.52	0.89	0.49	0.59	0.98	0.21	0.29	0.47
Region 4	0.56	0.73	1.22	0.67	0.80	1.30	0.39	0.51	0.87	0.48	0.57	0.92	0.32	0.43	0.63

This manuscript was accepted by Phys. Fluids. Click here to see the version of record.

For each Reynolds number, two experimental runs were performed and total 21,834 images were acquired and processed to compute the flow statistics. The velocity components corresponding to the x and y directions were U and V for the time-averaged velocities, and u' and v' for the fluctuating velocities, respectively. The experimental images were processed by applying the advanced multi-pass, multi-grid PIV algorithms implemented in an in-house PRANA code[63,64]. The robust phase correlation algorithm[65] was used to cross-correlate experimental images that could reduce bias errors and peak locking effects compared with the standard cross-correlation algorithm when applied to flows with high shear and rotational motion[66]. The PIV processing consisted of three passes, which started with an interrogation window of 64×64 pixels and ended with an interrogation window of 32×32 pixels. The initial and final iterations had a 50% and 75% window overlap, respectively, yielding the final total of 127×127 vectors with a gap spacing between two adjacent vectors of 0.34 mm. The particle displacements initially estimated from the first iteration were then used to shift the interrogation window in the next iteration. In all the iterations, particle displacements were computed from the cross-correlation map with a Gaussian peak fit for subpixel accuracy[58]. Vector validation was performed using a median filter[67] to remove spurious vectors and then fill in the blanks via interpolation.

1. *Estimated uncertainties of TR-PIV measurements*

For all the TR-PIV measurements of the studied Reynolds numbers, the percentage of detected spurious vectors, which was computed as the number of vectors that failed the validation process in the final iteration and averaged over the number of velocity vector fields, was less than 2%. The performance and uncertainty of the PRANA code have been thoroughly evaluated in the studies of[68],[69],[70], and[71]. These authors reported that the overall uncertainty of the PRANA code is approximately 0.1 pixels.

In this study, we followed the PIV uncertainty propagation proposed by[72] to estimate the experimental uncertainties, e, for the first and second order statistical quantities, including mean velocities, root-mean-square (RMS) fluctuating velocities, and Reynolds stress components. Besides, the experimental uncertainties estimated for the Reynolds numbers of Re_1, Re_2, and Re_3 were denoted as e_{Re_1}, e_{Re_2}, and e_{Re_3}, respectively. Table I summarizes the estimated uncertainties of the statistical results obtained from the TR-PIV measurements on Regions 1, 2, 3 and 4 for various Reynolds numbers. The uncertainties given in Table I are the maximum values normalized by the interstitial velocity U_m. It can be seen that for any region considered in this study, say for e.g. Region 1, the estimated uncertainties e_{Re_1}, e_{Re_2}, and e_{Re_3}, corresponding to Re_1, Re_2, and Re_3 have shown the trend of increase with increase in Reynolds numbers. Overall, the estimated uncertainties of the mean velocities were less than 2%, while those of the RMS fluctuating velocities and Reynolds stress were less than 1%. In the studies of[73] and[74], the authors argued that the quantification of uncertainty for instantaneous velocity and its derivatives is still difficult to address because it is related to various experimental parameters, such as time interval, tracer density, image calibration, and out-of-plane particle displacement, and processing algorithms, such as the interrogation window and cross-correlation algorithms.

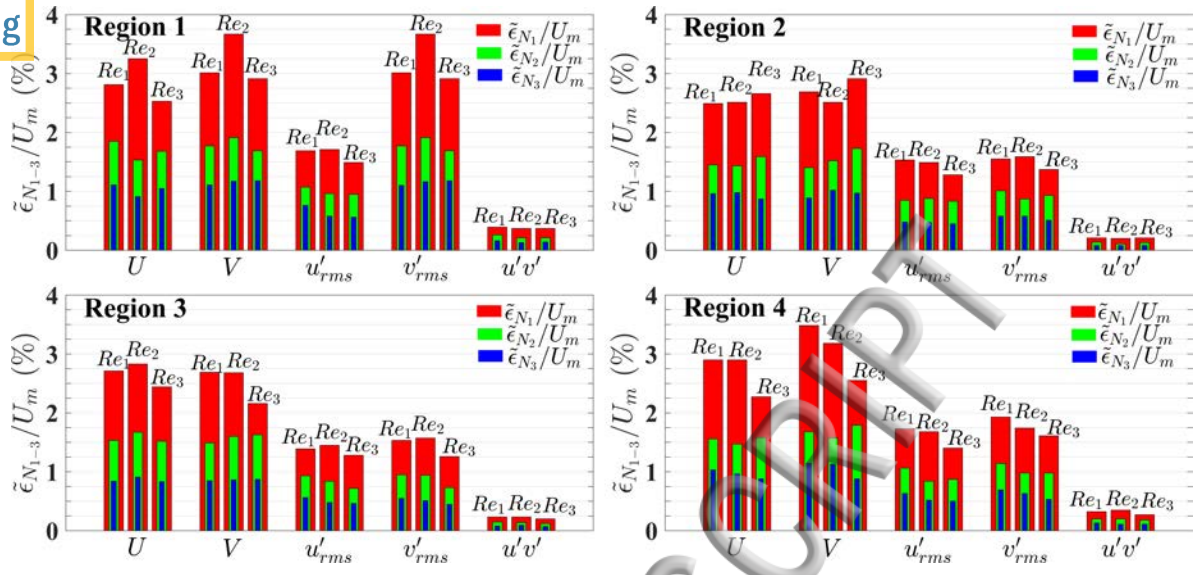

FIG. 2. Assessments on the convergence of the statistical results, i.e. U/U_m, V/U_m, u'_{rms}/U_m, v'_{rms}/U_m, and $u'v'/U_m^2$, obtained from TR-PIV measurements on Regions 1, 2, 3, and 4 for Re_1, Re_2, and Re_3. For each Reynolds number, heights and colors of the bar graphs represent $\tilde{\varepsilon}_{N_{1-3}}/U_m$ values computed using $N_1 = 5{,}000$, $N_2 = 10{,}000$, and $N_3 = 15{,}000$ velocity snapshots, respectively. Values computed for Regions 1 and 2 are summarized in Table II.

III. Results from the TR-PIV measurements

A. Convergence of the statistical results from the TR-PIV measurements

For the velocity measurements at each measurement region shown in Figure 1(b) and for each studied Reynolds number, a total of $N_{max} = 21{,}834$ instantaneous velocity vectors were obtained from the TR-PIV measurements that could be used to compute the flow statistics. In this section, we assess the convergences of the first- and second-order flow statistics, i.e., mean velocity, RMS fluctuating velocity, and Reynolds stress, which were computed using different numbers of velocity snapshots, i.e., the first 5,000 (N_1); the first 10,000 (N_2); the first 15,000 (N_3), and total (N_{max}). For these assessments, we followed the comparative approach discussed in the works of[60], and[61] by defining ε_{N_1}, ε_{N_2}, and ε_{N_3} as the absolute differences between the statistical results computed using N_1, N_2, and N_3 velocity snapshots and those computed using the entire set of velocity vector fields, i.e., N_{max}. In addition, $\tilde{\varepsilon}_{N_1}$, $\tilde{\varepsilon}_{N_2}$, and $\tilde{\varepsilon}_{N_3}$ are defined as the spatially averaged values of the corresponding differences over all grid points in the PIV velocity fields. This can be expressed as

$$\tilde{\varepsilon}_{N_j} = \frac{1}{M}\sum_{i=1}^{M} |\,(S_i)_{N_j} - (S_i)_{N_{max}}\,| \tag{3}$$

where $j = (1,2,3)$, M is the number of spatial points in the PIV velocity fields, and S_i represents the first- and second-order statistical results computed using the corresponding sets of N_1, N_2, N_3, and N_{max} velocity snapshots. The bar graphs in Figure 2 illustrate the normalized values of $\tilde{\varepsilon}_{N_1}$, $\tilde{\varepsilon}_{N_2}$, and $\tilde{\varepsilon}_{N_3}$ computed along measurement Regions 1, 2, 3, and 4 for the TR-PIV statistical results, i.e., U,

This manuscript was accepted by Phys. Fluids. Click here to see the version of record.

U, V, u'_{rms}, v'_{rms}, and $u'v'$. In addition, Table II summarizes the values of $\tilde{\varepsilon}_{N_1}/U_m$, $\tilde{\varepsilon}_{N_2}/U_m$, and $\tilde{\varepsilon}_{N_3}/U_m$ for the mean velocities, and RMS fluctuating velocities obtained from the TR-PIV measurements along Regions 1 and 2 for Reynolds numbers Re_1, Re_2, and Re_3. Results presented as bar graphs in Figure 2 could be interpreted as follows. For each flow region, convergences of the statistical results, including U, V, u'_{rms}, v'_{rms}, and $u'v'$, were assessed for TR-PIV velocity snapshots obtained at three Reynolds numbers Re_1, Re_2, and Re_3. For each Reynolds number, values of $\tilde{\varepsilon}_{N_1}/U_m$, $\tilde{\varepsilon}_{N_2}/U_m$, and $\tilde{\varepsilon}_{N_3}/U_m$ were accordingly illustrated by the colors and heights of bars. It can be seen from Figure 2 and Table II that for any specific Reynolds number and statistical quantity, values of $\tilde{\varepsilon}_{N_1}$, $\tilde{\varepsilon}_{N_2}$, and $\tilde{\varepsilon}_{N_3}$ decrease considerably when the number of velocity snapshots applied to calculate the statistical results increase from N_1 to N_3. Similar assessments on the convergences of the TR-PIV statistics obtained from Regions 3 and 4 were also performed. Those results are not shown here; however, we observed the similar trends in the convergence of the TR-PIV statistical results when the number of velocity vector fields increased. Furthermore, the values of $\tilde{\varepsilon}_{N_3}/U_m$ were found to be less than 1.2% for all the flow statistics computed along Regions 1, 2, 3, and 4 and for all three different Reynolds numbers considered in this study. This confirms the convergences of statistical results obtained from the TR-PIV velocity measurements. The TR-PIV statistical results presented hereinafter were computed using all of the available velocity snapshots, N_{max}.

B. Statistical results from the TR-PIV measurements

In this section, we discuss the TR-PIV statistical results, i.e., mean velocity, RMS fluctuating velocity, and Reynolds stress, obtained from the velocity measurements on Regions 1, 2, 3, and 4 for three Reynolds numbers Re_1, Re_2, and Re_3.

TABLE II. Convergences of the statistical results obtained via the TR-PIV measurements computed on Regions 1 and 2 for Re_1, Re_2, and Re_3. $\tilde{\varepsilon}_{N_1}$, $\tilde{\varepsilon}_{N_2}$ and $\tilde{\varepsilon}_{N_3}$ are the spatially averaged values of the absolute differences between the statistical results computed using $N_1 = 5{,}000$, $N_2 = 10{,}000$, $N_3 = 15{,}000$, and N_{max} velocity snapshots.

Region 1	$\tilde{\varepsilon}_{U/U_m}$ (%)			$\tilde{\varepsilon}_{V/U_m}$ (%)			$\tilde{\varepsilon}_{u'_{rms}/U_m}$ (%)			$\tilde{\varepsilon}_{v'_{rms}/U_m}$ (%)		
	N_1	N_2	N_3	N_1	N_2	N_3	N_1	N_2	N_3	N_1	N_2	N_3
Re_1	2.81	1.85	1.11	3.01	1.77	1.11	1.69	1.07	0.76	1.76	1.21	0.80
Re_2	3.25	1.53	0.91	3.67	1.91	1.17	1.71	0.96	0.58	1.64	1.00	0.62
Re_3	2.53	1.68	1.05	2.91	1.69	1.18	1.49	0.95	0.56	1.59	0.89	0.58
Region 2	$\tilde{\varepsilon}_{U/U_m}$ (%)			$\tilde{\varepsilon}_{V/U_m}$ (%)			$\tilde{\varepsilon}_{u'_{rms}/U_m}$ (%)			$\tilde{\varepsilon}_{v'_{rms}/U_m}$ (%)		
	N_1	N_2	N_3	N_1	N_2	N_3	N_1	N_2	N_3	N_1	N_2	N_3
Re_1	2.49	1.45	0.96	2.69	1.40	0.89	1.53	0.85	0.48	1.55	1.01	0.58
Re_2	2.51	1.43	0.98	2.51	1.52	1.02	1.49	0.88	0.47	1.59	0.87	0.58
Re_3	2.66	1.59	0.87	2.91	1.73	0.97	1.28	0.83	0.45	1.37	0.93	0.51

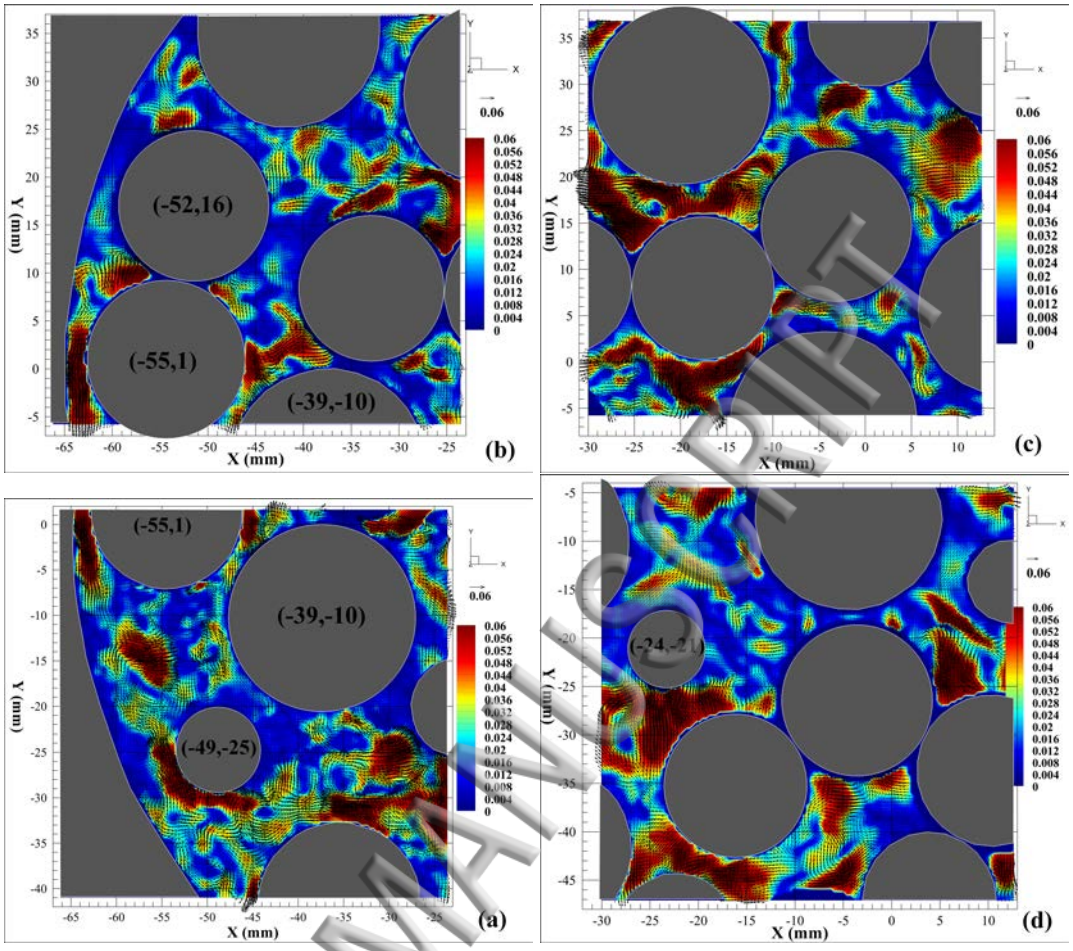

FIG. 3. Results from the TR-PIV measurements on (a) Region 1, (b) Region 2, (c) Region 3, and (d) Region 4 for Re_1. Instantaneous velocity vectors (m/s) and the color contour of the velocity magnitude values (m/s) are shown. Coordinates of spheres' centers are indicated.

Figure 3 illustrates the instantaneous results, including the velocity vectors and velocity magnitude contours, obtained from the TR-PIV measurements on Regions 1, 2, 3, and 4 for Re_1. It can be seen from the instantaneous in-plane velocity vectors shown in Figure 3 that the flow patterns in the transverse plane are very complex and reveal swirling structures aligned with the main axial flow (z-direction). The main flow is perpendicular to the cross-sectional plane along which the measurements were made. In Figure 4, the mean velocity vector fields and color contours of the mean velocity magnitude values obtained from TR-PIV measurements in Regions 1, 2, 3, and 4 are illustrated. Because the spheres were randomly packed within the test section, the spatial gaps between the neighboring spheres, and between the spheres and enclosure wall varied from 0 to nearly d_p. Such a random distribution of porosity within the packed spheres created various flow patterns within the spheres' spatial gaps. For instance, though a strong bypass flow was created near the sphere, whose center is at $(x_c = -55, y_c = 1)$, and the wall, the flow seemed to be stagnant within the gap of the neighboring sphere at $(x_c = -52, y_c = 16)$ and the enclosure

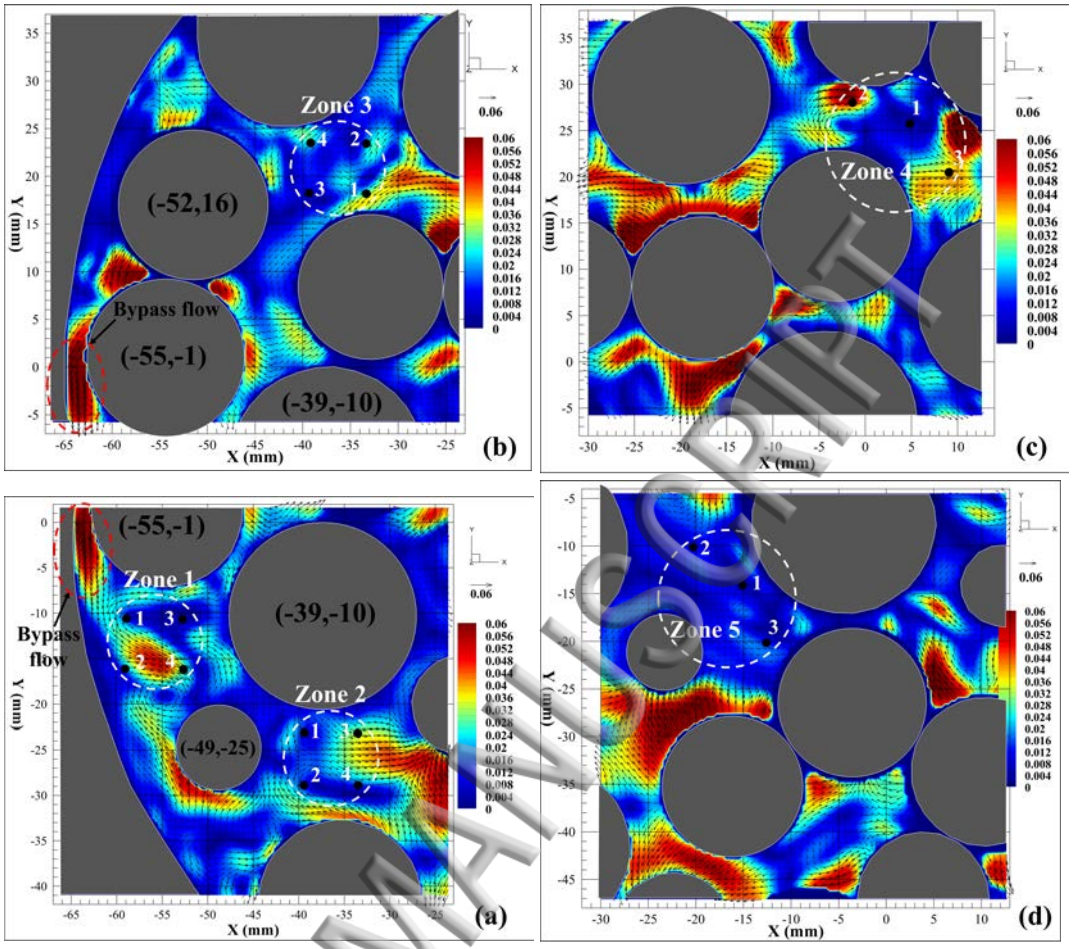

FIG. 4. Mean in-transverse plane velocity vectors (m/s) and color contours of the mean velocity magnitude values (m/s) computed from the TR-PIV measurements for Re_1 along *(a)* Region 1, *(b)* Region 2, *(c)* Region 3, and *(d)* Region 4. Vectors were de-sampled for better visibility. Coordinates of spheres' centers are indicated.

(c.f. Figure 4). When this strong bypass flow was ejected into a larger gap created by the wall and two other spheres, namely those at $(x_c = -39, y_c = -10)$ and $(x_c = -49, y_c = -25)$, it interacted with the counter bypass flow in the opposite direction, indicated by a low-velocity zone near the wall. Adjacent to this low-velocity zone, a re-circulation flow region was created because the bypass flows deflected and entered the large spatial gap. As shown in Figure 4, different flow patterns occurred in other spatial gaps with approximately equal sizes. For example, within the gap of $(-45 < x < -20, -35 < y < -20)$ created by a cluster of spheres, two strong flows in the transverse plane impinged on the sphere at $(x_c = -24, y_c = -21)$ and created a large circulation bubble that stretched along the x-direction. In addition, the flow patterns surrounding the cluster of spheres located within the gap of $(-35 < x < -10, 10 < y < 20)$ revealed impinging flows in the transverse plane.

Figure 5(a-b) displays the first-order statistics, i.e. mean velocity vectors and color contours of

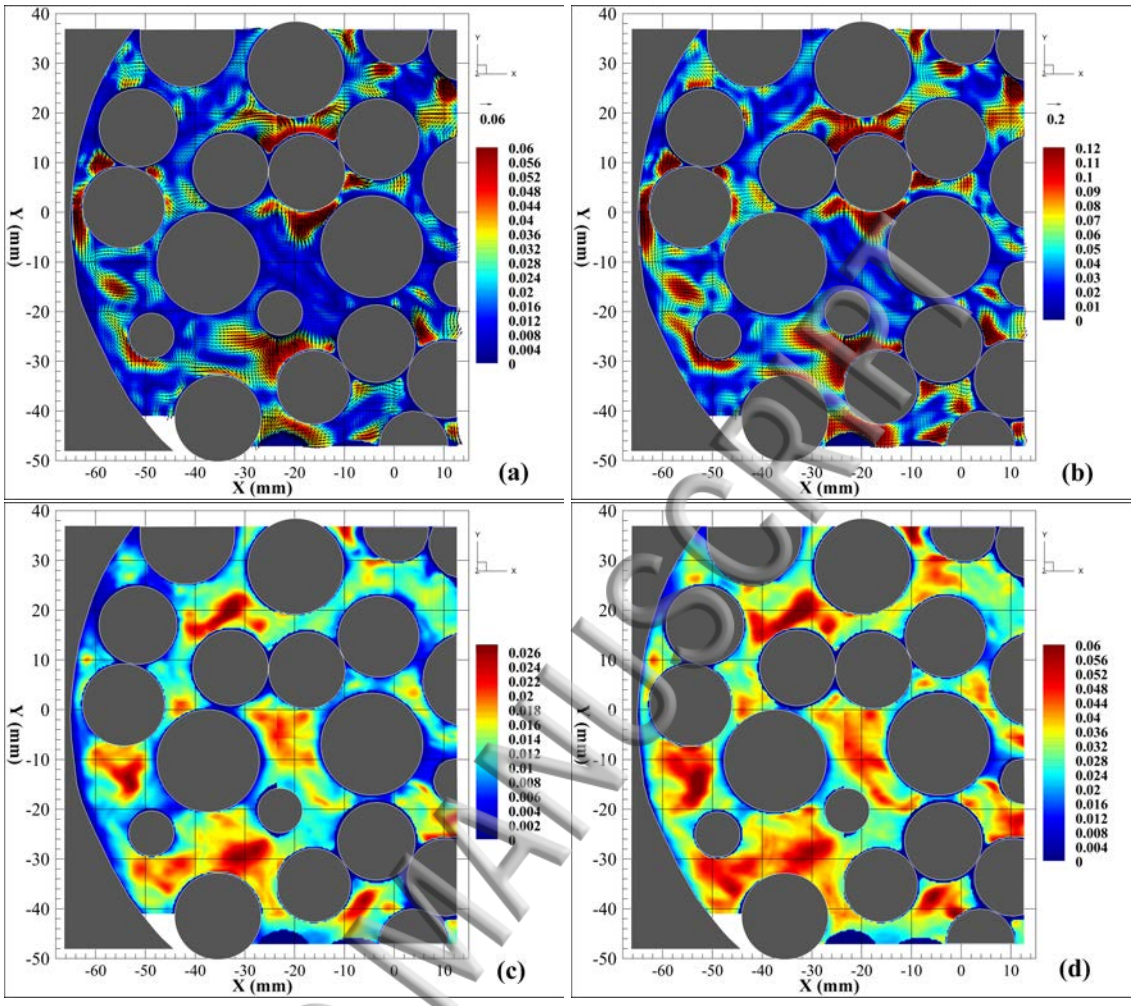

FIG. 5. Experimental results obtained TR-PIV measurements in the facility of randomly packed spheres for Re_1 (a)-(c) and Re_3 (b-d). Results from Regions 1, 2, 3, and 4 are adjoined for larger field of views. (a)-(b) Mean velocity vector (m/s) and velocity magnitude contour (m/s), (c)-(d) RMS fluctuating velocity, u'_{rms} (m/s).

the velocity magnitude values, whereas Figure 5(c-d) illustrate color contours of the second-order statistics, i.e., RMS fluctuating velocity u'_{rms}. The RMS fluctuating velocity v'_{rms} and Reynolds stress $u'v'$ are shown in Figure 6. In Figures 5 and 6, the TR-PIV experimental results obtained from Regions 1, 2, 3, and 4 were adjoined to obtain a larger field of view and are presented for Reynolds numbers Re_1 and Re_3. It can be seen in Figure 5 that the time-averaged velocity fields obtained from Re_1 and Re_3 showed similar flow structures. Moreover, the color contours of the turbulence statistics obtained from the TR-PIV measurements for low and high Reynolds numbers shown in Figure 5(c-d) and Figure 6(a-b) revealed similar flow maps.

We noticed that as the Reynolds number increased, the color contours of u'_{rms} and v'_{rms} were more widely distributed and had higher magnitude peaks. For instance, the color contour of u'_{rms} at Re_1 depicted peak values of 0.024 m/s and 0.021 m/s for the flow regions within the gaps

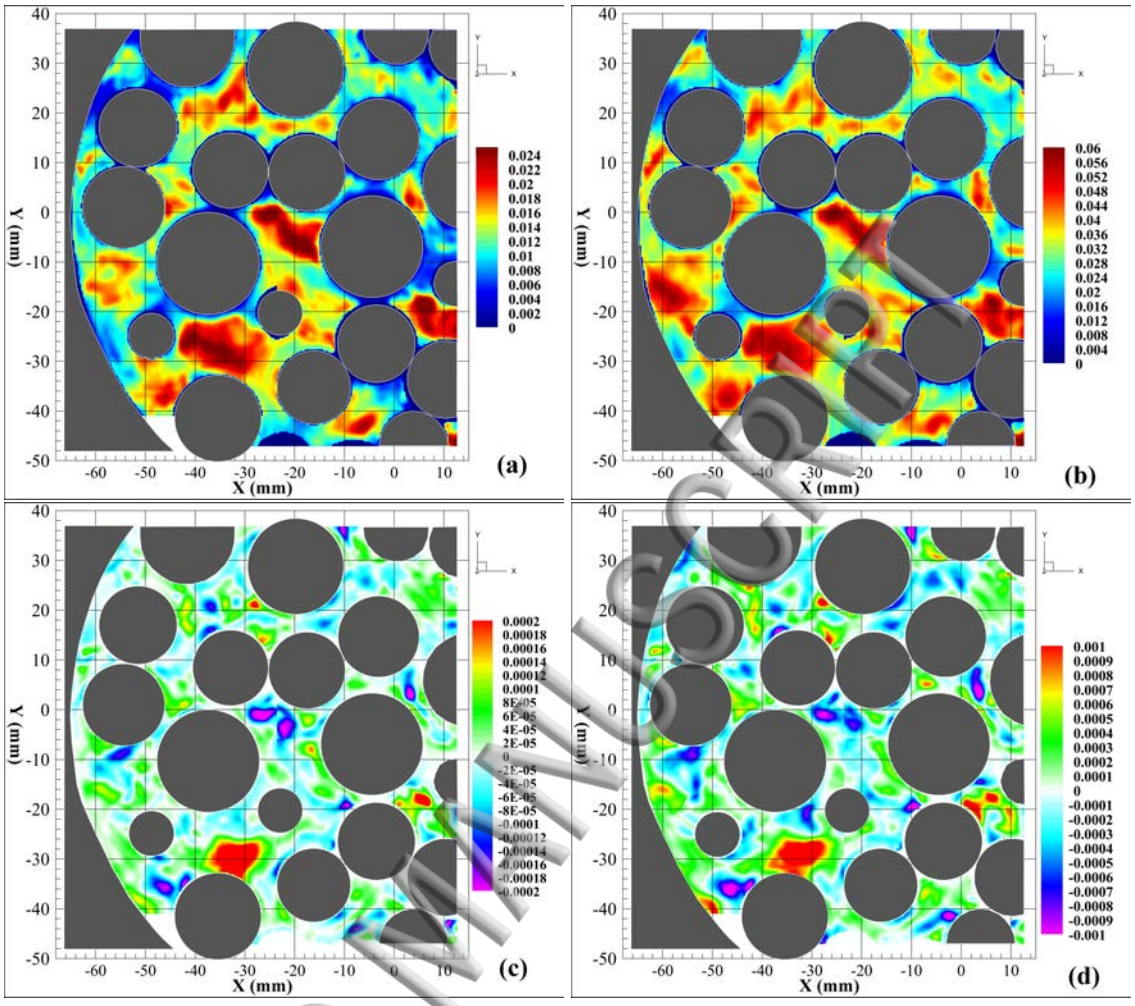

FIG. 6. Experimental results obtained from the TR-PIV measurements in the facility of randomly packed spheres for Re_1 (a)-(c) and Re_3 (b-d). Results from Regions 1, 2, 3, and 4 are adjoined to obtain a larger field of view. (a)-(b) RMS fluctuating velocity, v'_{rms} (m/s), and (c)-(d) Reynolds stress, $u'v'$ (m^2/s^2).

of $(-60 < x < 50, -20 < y < -10)$ and $(-50 < x < -40, -40 < y < -30)$, respectively. At higher Reynolds number Re_3, the peak values of u'_{rms} within these flow gaps were 0.062 m/s and 0.052 m/s, respectively. Similarly, within the flow gaps of $(-40 < x < -30, 20 < y < 30)$ and $(-45 < x < -30, -30 < y < -20)$, the v'_{rms} contours respectively showed peak values of 0.017 m/s and 0.026 m/s at Re_1, while they depicted higher values of 0.044 m/s and 0.056 m/s at Re_3. It is noted that the peak values of u'_{rms} and v'_{rms} were found to increase approximately at the same ratio as the increase in Reynolds number.

In the color maps of $u'v'$, the appearances of recirculation flow regions and shear layers created within the spatial gaps between the spheres and the wall are in accordance with the negative-positive values of $u'v'$, whose magnitudes considerably increased at higher Reynolds numbers. In the LES simulations of[30], the author showed that spheres with locally high temperature (hot spots) on their surfaces were found to have low levels of turbulence statistics, i.e., RMS fluctuating

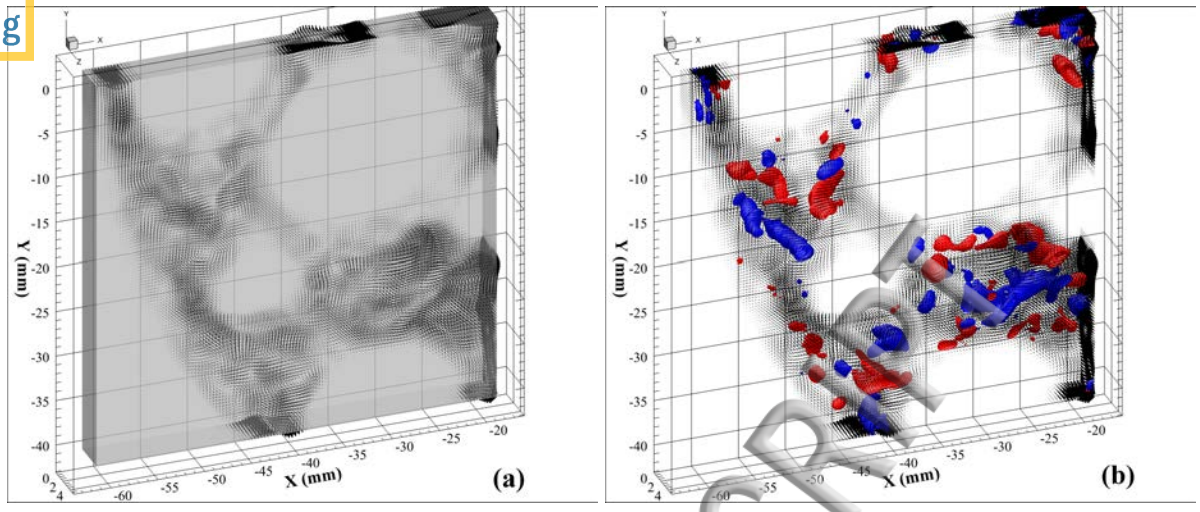

FIG. 7. Visualization of vortical structures by applying Taylor's hypothesis to the TR-PIV velocity measurements on Region 1 for Re_1. (a) Reconstructed quasi-instantaneous 3D velocity vector fields, (b) quasi-instantaneous 3D vortical structures identified by iso-surfaces of normalized z-vorticity, $\Omega_z \times d_p/U_m$. Positive *(red)* and negative *(blue)* iso-surfaces corresponding to normalized vorticity values of ± 6 are shown.

velocities and Reynolds stresses, in the surrounding fluid regions. In addition,[30] discussed that hot spot regions could be created where flow separations and circulations occurred.

C. Visualization of vortical structures by applying Taylor's hypothesis

In this section, the application of Taylor's frozen field hypothesis to the collection of TR-PIV velocity vector fields to reconstruct the quasi-3D vortical structures evolving within the spatial gaps of spheres distributed in Regions 1, 2, 3, and 4 is discussed. The visualization of vortical structures created and developed within the pores is meaningful to understand the flow mixing in packed beds.

In Taylor's frozen flow hypothesis, vortical flow structures are assumed to remain unchanged as they move downstream[75,76]. Uses of Taylor's hypothesis to reconstruct vortical structures can be reviewed in studies of[76],[77],[78],[79], and[61]. In those studies, quasi-instantaneous volumetric velocity data were built using the transformation on the axial z-direction defined as $\partial/\partial t = U_c \partial/\partial z$, where U_c is the convection velocity within the packed beds. In this study, following the approach used in these previous studies, we used the flow transformation in the z-direction with a uniform convective velocity such that $z^* = U_c t$, where t is the time interval between the first and a given velocity snapshot in the time-resolved velocity vector fields.

Figure 7(a) illustrates the 3D quasi-instantaneous velocity vector fields built by applying Taylor's hypothesis to the TR-PIV measurements on Region 1 for Re_1. The volumetric velocity fields were built from 150 instantaneous PIV velocity snapshots and the convection velocity of $U_c = 0.6U_m$. Prior to identification of the vortical structures, the instantaneous velocity vectors were smoothened by using the discrete cosine transform (DCT)-based penalized least squares (PLS) method[80], which has been proposed for post-processing PIV vector fields[81]. The vortical

structures were then extracted from the reconstructed volumetric velocity fields by applying a threshold for vorticity magnitude, as is similarly done in the studies of[76],[77],[79], and[61]. Figure 7(b) shows the vortical structures that were extracted from the flows in Region 1 and for Re_1, and identified by the iso-surfaces of the normalized z-vorticity $\Omega_z \times d_p/U_m$, where iso-surfaces correspond to positive and negative values, i.e. ± 6, of the normalized vorticity. It can be seen from Figure 7(b) that vortical flow structures were created and evolved within the spatial gaps between neighboring spheres and between the spheres and the wall.

Figure 8 illustrates a collection of vortical structures extracted from the quasi-instantaneous velocity vector fields that were obtained from the TR-PIV measurements on Regions 1-4 for Reynolds number of Re_3. Vortical structures were similarly extracted from TR-PIV velocity vector fields obtained for Reynolds numbers Re_1 and Re_2 to study the interactions of vortices within the spatial gaps of spheres. The results, however, are not shown here. The non-uniformity of sizes of the instantaneous vortical structures showed dependence on the characteristic sizes of gaps, i.e., large structures were found in large gaps; and either small structures or no structures were observed in the small gaps of the channel flows between spheres. The shear layers created from the small gaps of the bypass flows in Regions 1 and 2 were stretched along the tangential direction. When they entered the large neighboring gaps, these stretched layers broke into smaller vortical structures that evolved as a pair of counter-rotating vortices (c.f. Figure 8). Similar pairs of counter-rotating vortices were also identified in other large spatial gaps between the spheres. However, very few small sized vortical structures were found within smaller gaps which formed as channel flows between two neighboring spheres.

The visualization of vortical structures reconstructed from the TR-PIV measurements in the cross-flow plane using Taylor's hypothesis could allow us to study interactions of 3D vortices and flow mixing within packed beds that, until now, could only be obtained from high-fidelity unsteady CFD simulations[29,33,35].

IV. Analysis of velocity-velocity cross-correlation

In this section, to provide an insight of the complex characteristics of flow mixing in various spatial gaps within packed beds, we compute two-point spatial velocity-velocity cross-correlations using the TR-PIV measurements on Regions 1, 2, 3, and 4 in the transverse plane at three Reynolds numbers Re_1, Re_2, and Re_3. Previous studies[60,82–84] have shown that cross-correlation functions can provide important knowledge about the sizes and shapes of coherent structures evolving within the studied flows.

The two-point velocity cross-correlation is expressed by

$$R_{uu}(\boldsymbol{x}_r, \boldsymbol{\eta}, \tau) = \frac{\langle \boldsymbol{u}'(\boldsymbol{x}_r, t) \times \boldsymbol{u}'(\boldsymbol{x}_r + \boldsymbol{\eta}, t + \tau) \rangle}{\sqrt{\langle \boldsymbol{u}'^2(\boldsymbol{x}_r, t) \rangle} \sqrt{\langle \boldsymbol{u}'^2(\boldsymbol{x}_r + \boldsymbol{\eta}, t) \rangle}}. \tag{4}$$

In the above equation, $\langle . \rangle$ is the ensemble-average operator applied over the number snapshots, $\boldsymbol{u}'$ represents the fluctuating velocity, τ is the time interval, $\boldsymbol{x}_r$ is the coordinates of the referenced measurement point, and $\boldsymbol{\eta}$ is the spatial separation between two measurements. In Eq. 4, the spa-

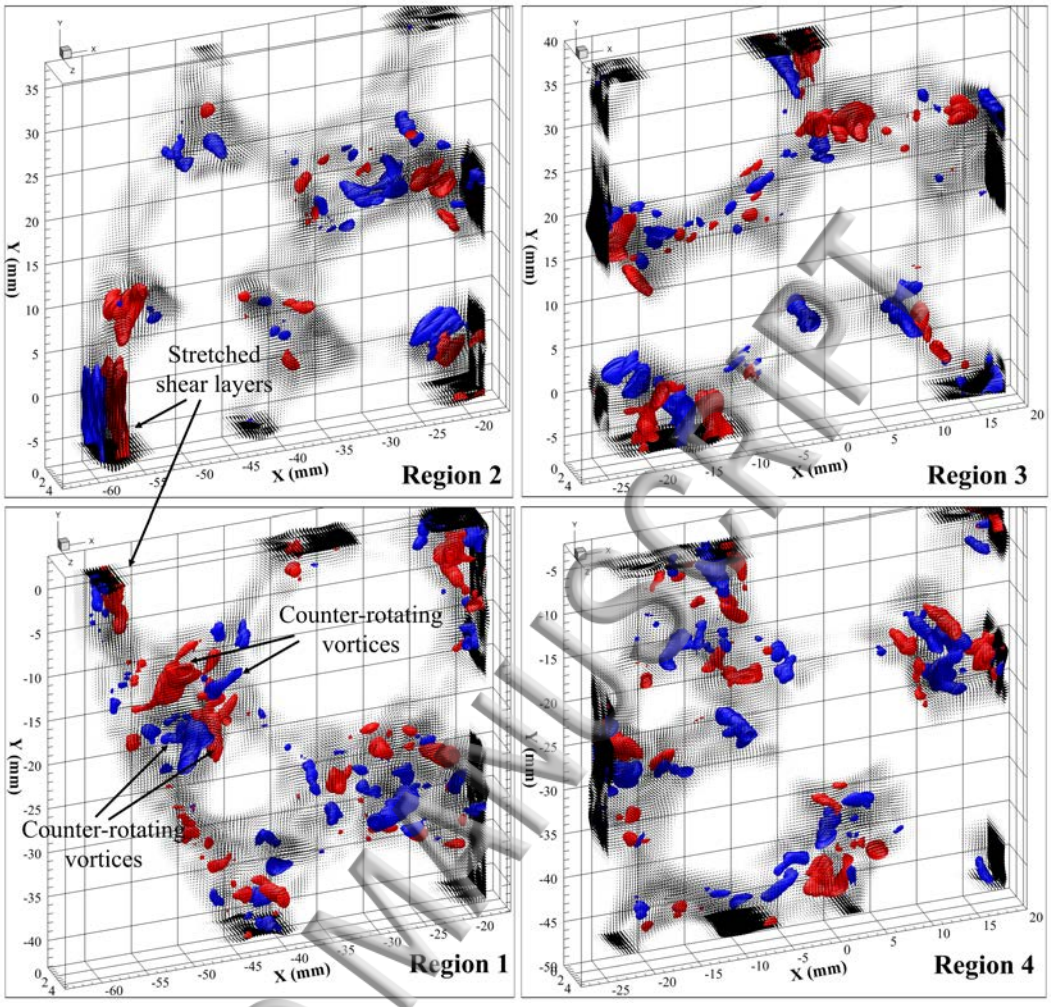

FIG. 8. Quasi-instantaneous 3D vortical structures identified by iso-surfaces of the normalized z-vorticity, $\Omega_z \times d_p/U_m$, for Re_3. Positive *(red)* and negative *(blue)* iso-surfaces correspond to ± 6.

tial velocity cross-correlation function is obtained when $\tau = 0$, which allows for the estimation of spatial correlation length scales, i.e., $R_{\boldsymbol{uu}0} = R_{\boldsymbol{uu}}(\boldsymbol{x}_r, \boldsymbol{\eta}, 0)$ as a function of the separation length $\boldsymbol{\eta}$. The maximum value of the correlation coefficient $R_{\boldsymbol{uu}0}$ is unity. Higher values closer to unity signify similar flow structures between two points under consideration. Lower correlation coefficient values closer to zero signify dissimilarities in flow structures between two points under consideration. The values of $R_{\boldsymbol{uu}0}$ indicate the spatial extent of correlated regions[85], allowing for the calculation of integral length scales as

$$^{k}L_{\boldsymbol{x}} = \int_0^{\infty} R_{\boldsymbol{uu}}(\boldsymbol{x}_r, \boldsymbol{\eta}_k, 0) d\boldsymbol{\eta}. \tag{5}$$

In the above equation, the superscript k expresses the direction of the separation vector along which the integration is computed, and $\boldsymbol{x}$ represents the velocity component. The integral length scale computed along the specific direction indicates the characteristic length scale of the flow eddies containing flow energy along that direction. Knowledge of the sizes and shapes of these flow

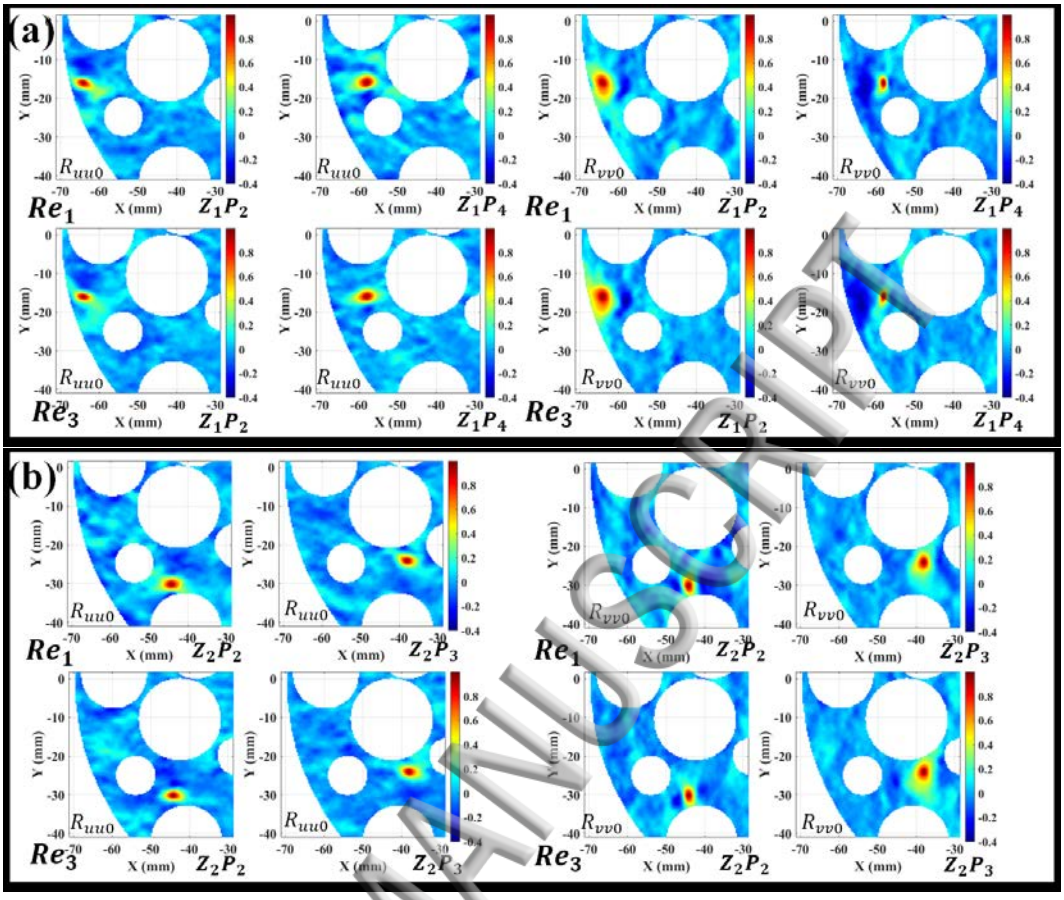

FIG. 9. Contour maps of the two-point spatial cross-correlations of the fluctuating velocities u' and v', i.e., R_{uu0} and R_{vv0}, computed using the TR-PIV velocity vector fields obtained in measurement Region 1 for (a) Zone 1 and (b) Zone 2 for Re_1 and Re_3.

eddies and their captured energy is important for gaining a better understanding of the flow mixing and heat transfer within the packed beds. For experimental measurements, the integral length scale ${}^{k}L_{\boldsymbol{x}}$ could be estimated by searching for the separation length at which $R_{\boldsymbol{uu}0} = 1/e \approx 0.37$[83,84,86].

In this study, the two-point cross-correlations R_{uu0} and R_{vv0} were calculated at different points located in several spatial gaps (or zones) between the spheres. For instance, each of Zones 1, 2, and 3 was formed by four points while Zones 4 and 5 were defined by three points as can be seen in Figure 4. Figure 9 and Figure 10 depict color maps of the two-point spatial cross-correlations of the fluctuating velocities, u' and v', computed at various points located in different measurement Regions 1-4 and Zones 1-5. For each spatial region, the results are presented for Reynolds numbers Re_1 and Re_3. It can be seen that the shapes and sizes of the spatial cross-correlations, i.e., R_{uu0} and R_{vv0}, are titled towards the flow direction in the transverse plane, indicating the effects of shearing caused by the mean velocity fields. For instances, the correlations R_{vv0} at Point 2 in Zone 1 (denoted as $Z1P2$), and Point 3 in Zone 2 (denoted as $Z2P3$, see Figure 9), and the correlation R_{uu0} at Point 1 in Zone 3 (noted as $Z3P1$, see Figure 10) displayed long trails following the mean flow patterns within the spatial gaps between neighboring spheres. The correlations R_{vv0} at $Z2P3$,

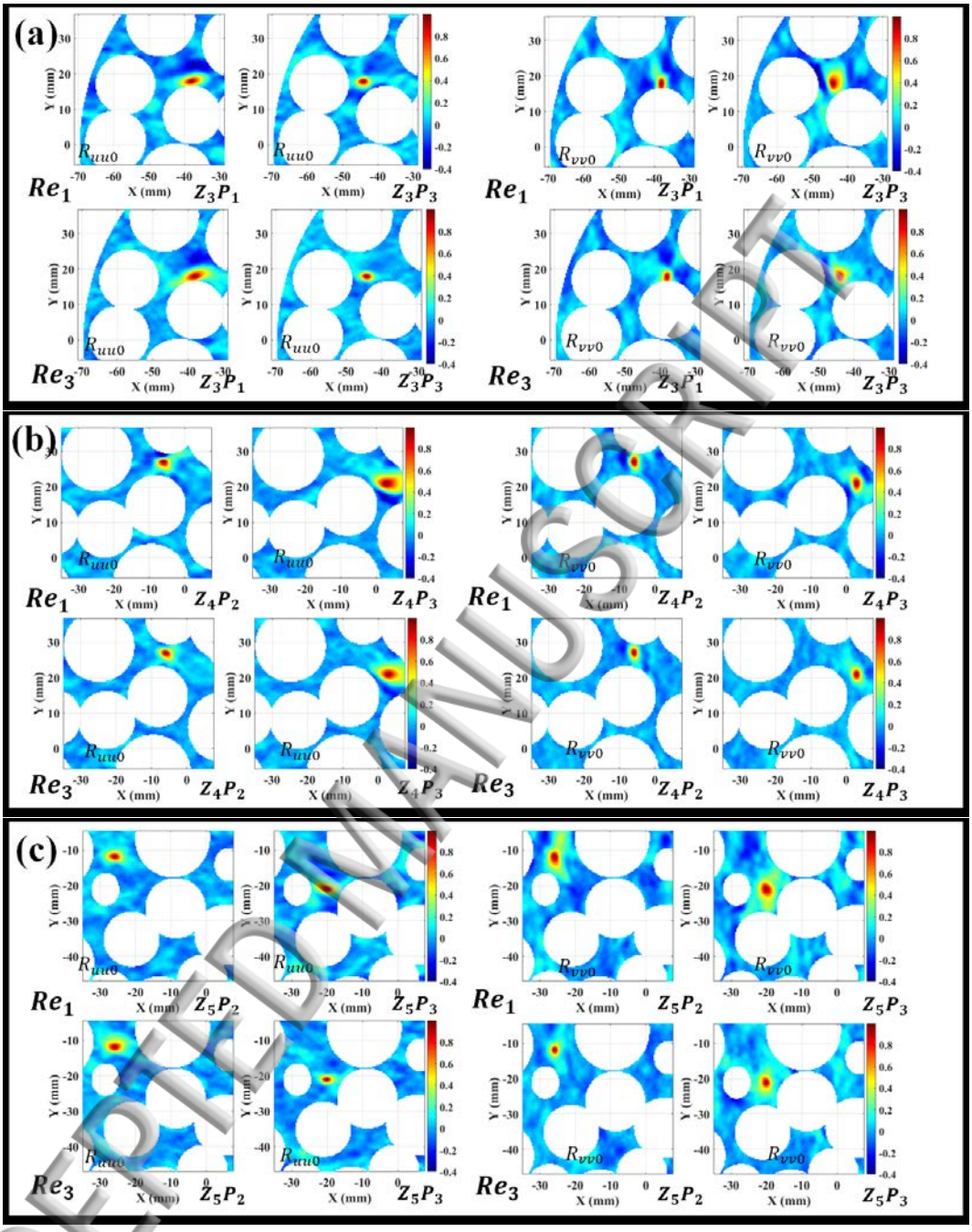

FIG. 10. Contour maps of the two-point spatial cross-correlations of the fluctuating velocity u' and v', i.e., R_{uu0} and R_{vv0}, computed using the TR-PIV velocity vector fields obtained in measurement Regions 2, 3, and 4 for (a) Zone 3, (b) Zone 4, and (c) Zone 5 for Re_1 and Re_3.

*Z*4*P*3 and *Z*5*P*3 had their shapes covering large spatial areas between the spheres, indicating that the local flows in those regions were highly correlated. For points located in the near-wall region of Zones 1 and 2, i.e., *Z*1*P*2 and *Z*2*P*2, the shapes of the correlations did not show significant changes when Reynolds number increased from Re_1 to Re_3. On the other hand, for points located in the far-

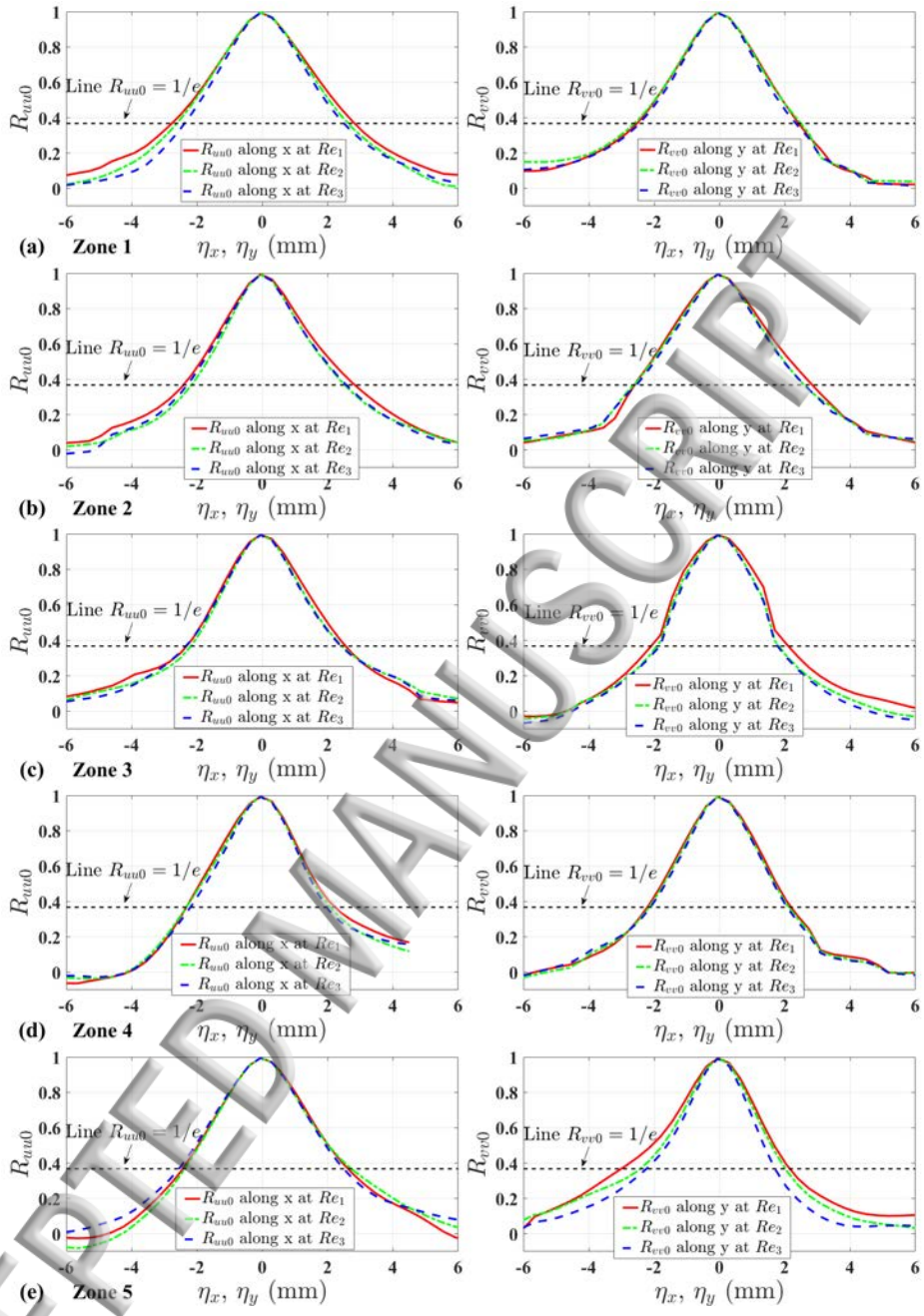

FIG. 11. Spatial turbulent velocity cross-correlations R_{uu0} and R_{vv0} computed at *(a)-(e)* Zones 1-5 using the TR-PIV velocity vector fields obtained from the MIR facility of randomly packed spheres for Reynolds numbers Re_1, Re_2, and Re_3. Note that correlations R_{uu0} and R_{vv0} were computed along x and y directions, and averaged over various points located in each zone. The integral length scales ${}^{k}L_{\boldsymbol{x}}$ were estimated by searching for the separation length at which $R_{\boldsymbol{uu}0} = 1/e \approx 0.37$.

wall regions of Zones 4 and 5, long trails can be seen in the correlation contours of R_{uu0} and R_{vv0}, and their spatial extents are reduced when the Reynolds number increased. Similar observations on the spatial correlations computed in the near-wall and far-wall regions were discussed in[50].

This manuscript was accepted by Phys. Fluids. Click here to see the version of record.

Figure 11 compares the cross-correlations R_{uu0} and R_{vv0} computed for Zones 1-5 for Re_1, Re_2, and Re_3. It is notated that for each zone, R_{uu0} and R_{vv0} were computed along x and y directions, and averaged over all points located in that area and for various Reynolds numbers. Figure 11(a-b) show that the R_{uu0} values computed in Zones 1 and 2 along x had their integral length scales ${}^{x}L_x$ decrease from 2.79 and 2.65 mm to 2.44 and 2.37 mm, respectively, when the Reynolds number increased from Re_1 to Re_3. On the other hand, the increase of Re yielded negligible changes in the ${}^{y}L_y$ value estimated from the R_{vv0} values. In Figure 11(c-d), integral length scales ${}^{x}L_x$ and ${}^{y}L_y$ were estimated to be approximately 2.20, 2.35, and 2.45 mm in Zones 3, 4 and 5, respectively. The effect of increasing Reynolds numbers did not have an influence on the estimated values of integral length scales, except for in Zone 5, where the ${}^{y}L_y$ values decreased from 2.58 mm to 1.98 mm when the Reynolds number increased from Re_1 to Re_3. In comparison with ${}^{x}L_x$ and ${}^{y}L_y$ computed from various spatial gaps between the spheres, the integral length scales obtained from Zones 1 and 2 were greater than those obtained from Zones 3, 4, and 5, indicating the effects of bypass flows in the vicinity of the wall.

V. Flow analysis by proper orthogonal decomposition

In this section, we discuss our flow analysis using proper orthogonal decomposition (POD) of the TR-PIV velocity snapshots to extract the dominant flow structures that play important roles in the flow dynamics and heat transfer of packed beds. Flow structures extracted from the velocity vector fields of Regions 1-4 for Reynolds numbers Re_1, Re_2, and Re_3 are discussed in this section.

A. Overview of proper orthogonal decomposition

[87] introduced POD or Karhunen-Loéve decomposition into turbulence research to identify statistically dominant flow features, i.e., coherent structures, in experimental data and numerical simulations. For a given flow, the velocity field $\boldsymbol{u}(\boldsymbol{x})$ is decomposed into a set of spatially orthogonal modes and a set of temporal coefficients, which vary, respectively, only in space and time. Spatial structures revealed by POD modes are considered as coherent structures or large-scale flow structures, which normally contain the most flow energy. Temporal evolutions of the POD modes are represented by the associated POD temporal coefficients. The POD modes extracted from the velocity vector fields yield an optimal representation of the flow field such that, for any given number of modes, the two-norm of the truncation error between the original velocity data and the projection of the original velocity data onto such modes is minimized[88,89]. In addition, the original velocity fields can be approximated or reconstructed using the few lowest-order POD modes that capture the highest amount of flow kinetic energy and the associated temporal coefficients. Detailed descriptions of the POD analysis can be reviewed in the works of[88],[89], and[90]. A brief review of the snapshot POD of the velocity fields is provided here. A POD analysis of a given velocity vector field $\boldsymbol{u}(\boldsymbol{x}, 0 \leq t \leq T)$ (T is a finite time direction) can be described as

$$\boldsymbol{u}(\boldsymbol{x},t) \cong \sum_{k=1}^{N} \zeta_k(t)\psi(\boldsymbol{x}), \tag{6}$$

This manuscript was accepted by Phys. Fluids. Click here to see the version of record.

where N is the number of velocity snapshots, and $\zeta_k(t)$ and $\psi(\boldsymbol{x})$ are the POD temporal coefficients and POD basis functions, respectively. $\psi(\boldsymbol{x})$ are computed as the eigenfunctions of a two-point correlation matrix $\boldsymbol{R}(\boldsymbol{x},\boldsymbol{x}')$ defined as

$$\boldsymbol{R}(\boldsymbol{x},\boldsymbol{x}') = \frac{1}{T}\int_0^T \boldsymbol{u}(\boldsymbol{x},t)\cdot\boldsymbol{u}(\boldsymbol{x}',t)dt. \tag{7}$$

It is common that the velocity vector fields obtained by experiments and numerical simulations are discrete, and the snapshot POD method[90] is usually used. In the current study, we applied the snapshot POD analysis to the collection of TR-PIV velocity vector fields obtained from Regions 1, 2, 3 and 4 corresponding to Reynolds numbers of Re_1, Re_2, and Re_3. First, a correlation matrix is defined as

$$C_{ij} = \frac{1}{N}\int \boldsymbol{u}(\boldsymbol{x},t_i)\cdot\boldsymbol{u}(\boldsymbol{x},t_j)d\boldsymbol{x}, \tag{8}$$

and the POD temporal coefficients and POD basis functions are computed as

$$\boldsymbol{\Psi}_k(\boldsymbol{x}) = \sum_{i=1}^{N}\alpha_{ki}\boldsymbol{u}(\boldsymbol{x},t_i)\zeta_k(t_j) = N\sum_{i=1}^{N}\alpha_{ki}C_{it_j}. \tag{9}$$

In the above equations, coefficients α_{ki} are defined as

$$\alpha_{ki} = \frac{\upsilon_i^k}{\sqrt{N\sum_{m=1}^{N}\sum_{r=1}^{N}\upsilon_m^k\upsilon_r^k C_{mr}}}, \tag{10}$$

where υ_i^k is the ith element of the eigenvector υ^k associated with the eigenvalue λ_k of the matrix $\boldsymbol{C}$. The correlation matrix $\boldsymbol{C}$ is built from instantaneous velocity snapshots, therefore, a derived eigenvalue λ_k associated with a POD mode k represents the flow kinetic energy contained by that mode.

B. Results from the POD velocity decomposition

The results from the POD analysis of the velocity fields obtained from the TR-PIV measurements on Regions 1 and 2 in the MIR facility of randomly packed spheres are presented in Figures

TABLE III. Flow kinetic energy fractions contained in the low-order POD modes obtained from POD velocity decomposition of the TR-PIV velocity vector fields for measurement Regions 1-4 and Reynolds numbers of Re_1, Re_2, and Re_3.

	Mode 1 (%)			Mode 2 (%)			Mode 3 (%)			Mode 4 (%)		
Region	Re_1	Re_2	Re_3	Re_1	Re_2	Re_3	Re_1	Re_2	Re_3	Re_1	Re_2	Re_3
1	56.6	54.3	55.3	2.39	1.80	1.94	1.44	1.58	1.46	1.25	1.41	1.12
2	64.3	62.6	60.5	2.31	1.47	1.71	1.65	1.18	1.36	1.36	1.11	0.98
3	74.4	70.9	69.9	1.20	1.14	1.20	1.14	1.02	0.86	0.84	0.77	0.78
4	64.6	60.4	61.3	1.60	1.41	1.29	1.36	1.29	1.12	1.27	1.19	1.10

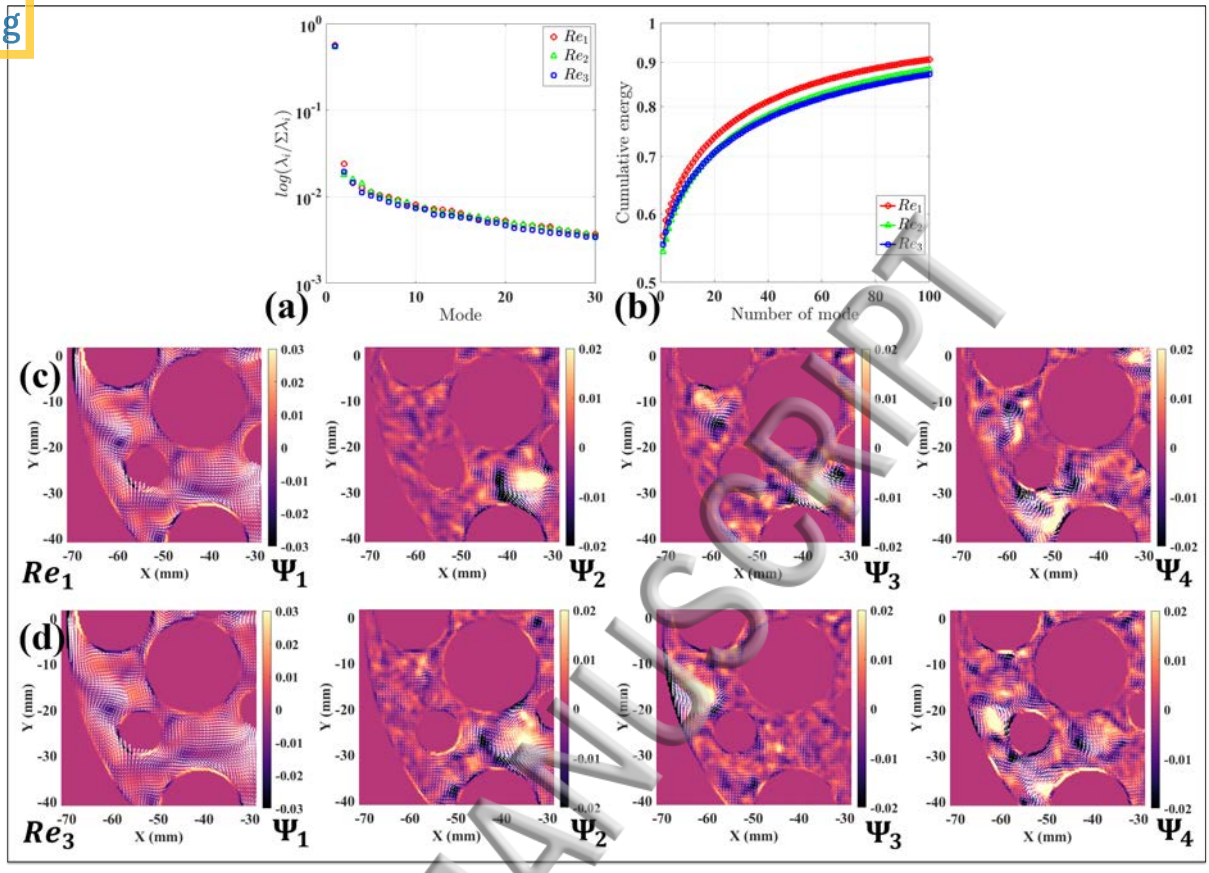

FIG. 12. POD analysis of the velocity fields obtained from the TR-PIV measurements on Region 1 for Re_1, Re_2, and Re_3. *(a)* Kinetic energy spectra; *(b)* cumulative energy. Low-order POD velocity modes, i.e., Ψ_1, Ψ_2, Ψ_3, and Ψ_4, for *(c)* Re_1 and *(d)* Re_3. Color shows vorticity calculated from the corresponding POD velocity basis function.

12 and 13. Results from the POD analysis on Regions 3 and 4 are not shown here, for the sake of brevity. Figures 12-13(a-b) show the energy spectra and the cumulative energy from the POD analysis of the TR-PIV velocity fields for Re_1, Re_2, and Re_3. The kinetic energy fractions contained in low-order POD modes 1, 2, 3, and 4 are listed in Table III for different measurement Regions 1-4 and for Reynolds numbers of Re_1, Re_2, and Re_3. For all four measurement regions, spatial flow structures revealed by the first POD modes were found approximately equivalent to the time-averaged velocity fields. Besides, the flow kinetic energy fractions of the first POD modes were found to decrease when the Reynolds numbers increased. For Regions 1, 2, 3, and 4, the first POD modes contained 56.6%, 64.3%, 74.4%, and 64.6%, of the total flow kinetic energy, respectively, at Re_1. However, when Reynolds number increased to Re_3, the kinetic energy levels captured by the first POD modes of Regions 1-4 decreased to 55.3%, 60.5%, 69.9%, and 61.3%, respectively. Moreover, for all cases, the kinetic energy levels of the low-order POD modes 2, 3, and 4 were less than 3%, resulting in the slow convergence of the cumulative kinetic energy. The total flow kinetic energy levels contained in the first 100 low-order POD modes at Re_3 were 87.2%, 89.2%,

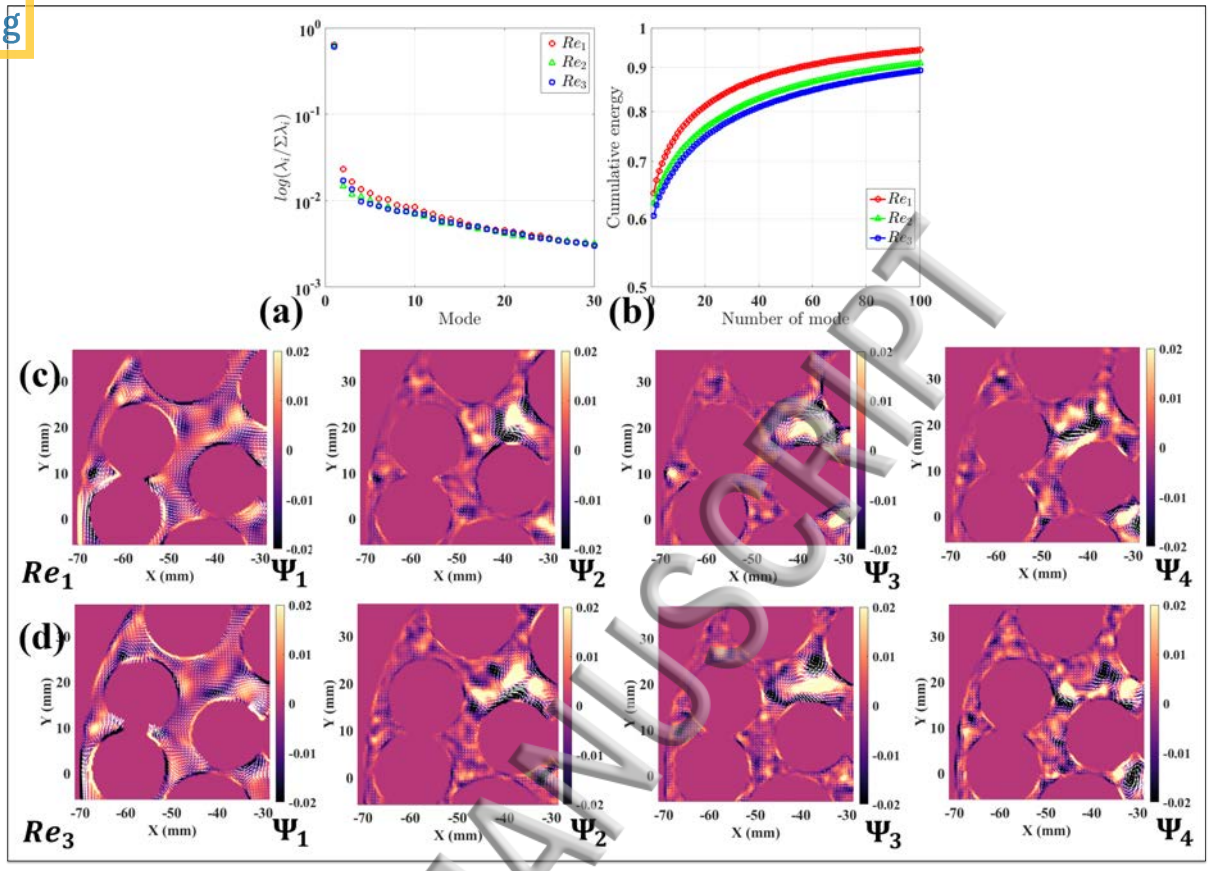

FIG. 13. POD analysis of the velocity fields obtained from the TR-PIV measurements on Region 2 for Reynolds numbers of Re_1, Re_2, and Re_3. *(a)* Kinetic energy spectra; *(b)* cumulative energy. Low-order POD velocity modes, i.e., Ψ_1, Ψ_2, Ψ_3, and Ψ_4, for *(c)* Re_1 and *(d)* Re_3. Color shows vorticity calculated from the corresponding POD velocity basis function.

91.6%, and 89.5% for Regions 1-4, respectively. The reduction of kinetic energy levels in the first POD modes when Reynolds numbers increased and the slow convergence of the cumulative energy indicate that flow mixing at higher Reynolds numbers for flow regions 1-4 is highly turbulent and the flow kinetic energy is widely distributed over many small-scale flow structures.

Figures 12-13(c-d) illustrate the in-plane components of the low-order POD modes 1, 2, 3, and 4 obtained from the velocity decomposition for Regions 1-4 and for Re_1 and Re_3. It should be noted that, in our POD velocity decomposition analysis, the POD spatial functions were non-dimensional. The first POD modes revealed the flow structures to be statistically similar to the mean velocity fields. For a given Reynolds number, the dominant flow structures depicted by the higher-order POD modes had smaller shapes and sizes compared with those revealed by the lower-order POD modes. Moreover, except for the flow structures shown by POD mode 1, the dominant flow structures revealed by POD modes 2, 3, and 4 for each measurement region were not entirely analogous. It is worth noting that the results obtained from the POD velocity decomposition also showed that the statistically dominant large-scale flow structures extracted using the POD basis

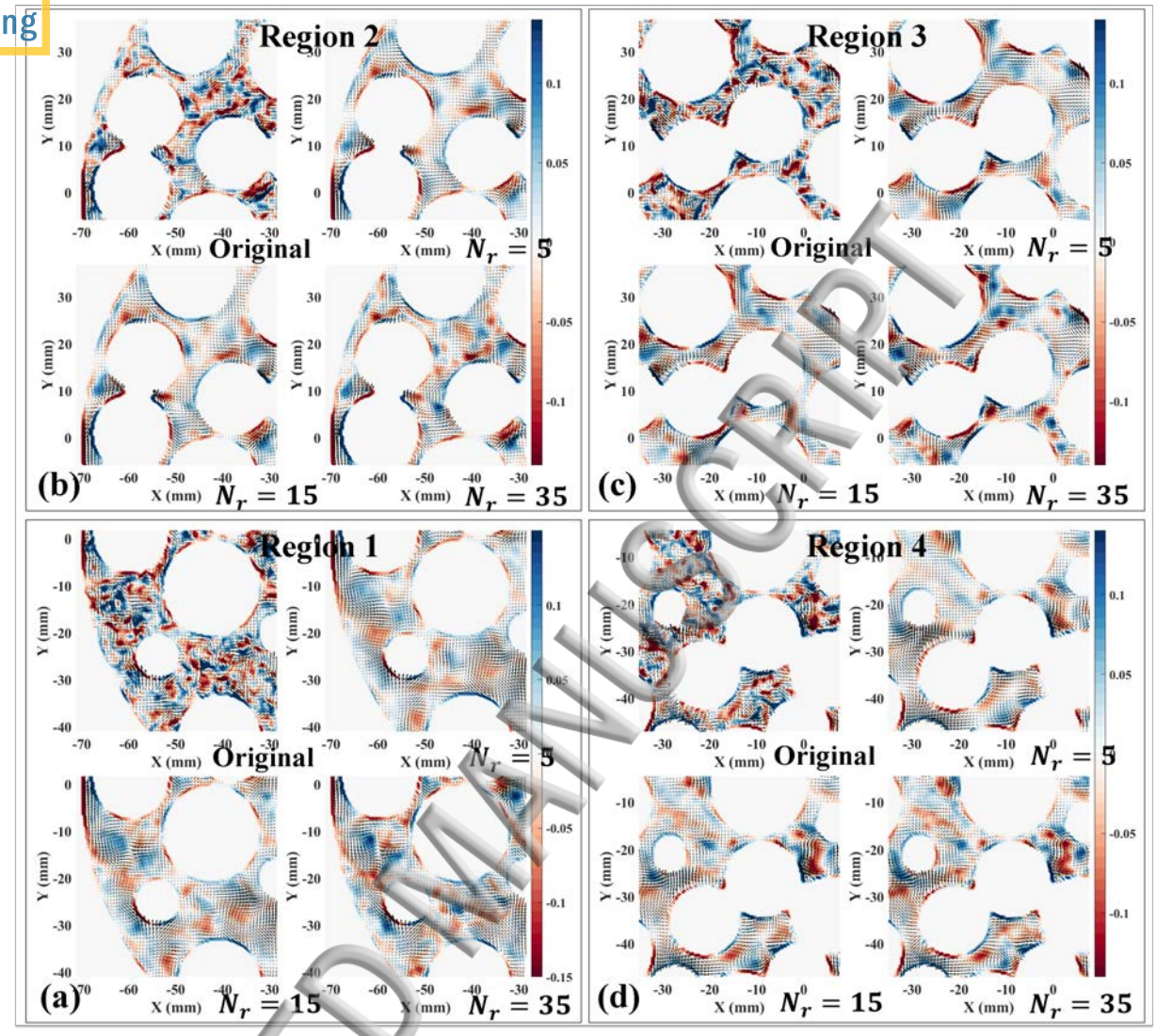

FIG. 14. Velocity reconstruction using low-order POD modes. Comparisons between the original instantaneous velocity snapshots obtained at Re_3 and those reconstructed using different N_r low-order POD modes, i.e., $N_r = 5$, 15, and 35 for *(a)* Region 1, *(b)* Region 2, *(c)* Region 3, and *(d)* Region 4 are shown. Color shows vorticity calculated from the in-plane velocity components.

functions had approximately equal shapes and sizes as the vortical structures illustrated by the iso-surfaces of vorticity shown in Figure 8. Such similarity demonstrates the capabilities of the two approaches for visualizing instantaneous large-scale flow structures via Taylor's hypothesis and statistically dominant flow structures via POD analysis. This could allow for further comparisons and validations between experiments and simulations that aim to study the 3D flow structures contributing to flow mixing in randomly packed spheres.

Figure 14 illustrates the capability of performing reduced-order reconstructions using low-order POD spatial modes and the associated POD temporal coefficients to reconstruct instantaneous velocity fields for different measurement Regions $1-4$, and at Reynolds numbers of Re_1 and Re_3.

In Figure 14, the original velocity fields and vorticity contours are shown and compared with those obtained from the low-order reconstructions using various N_r low-order POD modes, i.e., $N_r = 5$, 15, and 35. We found that the low-order reconstructed velocity and vorticity fields depict large-scale coherent flow structures, which are considered to contain the most flow kinetic energy. In addition, the flow reconstructed using higher numbers of POD modes revealed more flow details with smaller-scale coherent structures. It was also seen that when Reynolds numbers increased, it became necessary to use higher numbers of low-order POD spatial modes and the associated POD temporal coefficients to reconstruct the velocity and vorticity fields with small-scale flow structures. This can be explained by the distribution of flow kinetic energy over many small-scale flow structures at higher Reynolds numbers, as previously illustrated in the plots of the POD energy spectra.

The results obtained from the POD velocity decomposition allowed us to extract the coherent flow structures obtained from the TR-PIV measurements at the transverse plane in the MIR facility of randomly packed spheres. The POD spatial modes represent the large-scale flow structures that are orthogonal, and their associated orders are normally ranked by the amount of flow kinetic energy each of them contain. Hence, the POD analysis is beneficial in studies that aim to characterize flow structures associated with energy transfer between coherent large-scale structures to turbulent eddies[50]. In the next section, we will apply POD analysis and its low-order reconstruction capabilities to facilitate our study on identifying the vortices and their distributions in the measurement regions along the transverse plane.

VI. Identification and distribution of vortices in the transverse TR-PIV measurement plane

The use of Taylor's frozen hypothesis made it easier for us to visualize the quasi-vortical structures within the spatial gaps of packed beds as previously discussed in Section III C. In this section, we investigate the characteristics of these vortices, such as their populations, spatial distributions, and circulations, extracted from the TR-PIV velocity vectors on Region 1, 2, 3, and 4 along a transverse plane.

A. Overview of vortex identification using POD analysis

Several methods have been proposed to identify vortices for given velocity fields. Using results from a DNS of isotropic turbulence,[91] identified vortex structures based on vorticity magnitude. However, this method was not able to separate flow regions induced by vortex cores and shear motions. Later, more advanced and robust methods, such as the Q criterion[92], the Δ criterion[93], the λ_{ci} criterion[94], and the λ_2 criterion[95], were proposed to better distinguish the vortex cores against shear motions[96]. To extract a projection of 3D vortices on 2D planar velocity fields, which are typical for 2D2C PIV measurements,[97] introduced a modified λ_{ci} criterion, which is a 2D form of the 3D velocity gradient tensor.[98] applied a pattern recognition method to identify vortices in their PIV velocity fields based on a referenced eddy structure with Gaussian damping.[99] proposed a method based on a triple decomposition of motion, which was further enhanced by[100]. This method calculates a rigid-body-rotation vorticity, which acts as the local measure of vortex-related

vorticity and is able to separate the swirling motions of vortices from pure shearing motions. Detailed discussions and comparisons of various vortex identification methods can be reviewed in the works of[99] and[96].

In the current study, we employed the approach proposed by[101] to perform statistical analysis on a collection of PIV instantaneous velocity vector fields, and gained statistical information on the locations and circulations of vortical structures. This approach combines POD analysis and vortex identification algorithms. Details of this approach can be reviewed in the works of[101], and only brief information is provided here.

In their study,[101] the authors first performed POD analysis on PIV velocity vector fields obtained from a swirling flow in a circular duct, and used the low-order POD spatial modes and POD temporal coefficients to reconstruct the collection of instantaneous velocity snapshots. This allowed for the separation of large-scale flow structures, i.e., energy-containing eddies and revealed by the low-order POD modes, from the small-scale flow structures. The identifications of vortex centers and vortex cores were then performed on the low-dimensional reconstructed PIV velocity vector fields as follows. For a given fixed point P in the measurement domain, the non-dimensional scalar function Γ_1 at P is defined as

$$\Gamma_1(P) = \frac{1}{N}\sum_S \frac{(PM \wedge U_M)\cdot z}{\|PM\|\cdot\|U_M\|} = \frac{1}{N}\sum_S \sin(\theta_M) \tag{11}$$

where S is a 2D area surrounding P, point M is within S, z is the normal vector of the measurement region ($\|z\| = 1$), N is the number of points M inside S, and θ_M represents the angle between velocity vector UM and radius vector PM. $|\Gamma_1|$ has maximum value of 1 and reaches values ranging from 0.9 to 1 near the vortex center, which allows us to identify the center of vortical structures based on a threshold calculation[101].

Considering the local convection velocity $\tilde{U}_P$ around point P, the vortex boundary identification can be derived as

$$\Gamma_2(P) = \frac{1}{N}\sum_S \frac{\left[PM \wedge \left(U_M - \tilde{U}_P\right)\right]\cdot z}{\|PM\|\cdot\left\|U_M - \tilde{U}_P\right\|} \tag{12}$$

where $\tilde{U}_P = 1/S\int_S U dS$. For a 2D incompressible velocity field,[101] discussed that $|\Gamma_2|$ is Galilean invariant, and is a local function depending only on Ω and μ, where Ω is the rate of rotation tensor corresponding to the anti-symmetrical part of the velocity gradient ∇u, and μ is the eigenvalue of the symmetrical part of ∇u.[101] have shown that in the region where the flow is locally dominated by rotation, i.e. $|\Omega/\mu > 1|$, $|\Gamma_2 > 2/\Pi|$, which was chosen as a threshold to define the vortex core region and used to estimate the area and circulation of detected vortices.

B. Results and discussions on vortex characteristics

We applied the combined approach briefly described above to the collections of TR-PIV instantaneous velocity vector fields acquired at Regions 1, 2, 3, and 4, and for three Reynolds numbers Re_1, Re_2, and Re_3. For each measurement region and each Reynolds number, the statistical information of the vortices was analyzed from $N_{max} = 21{,}834$ velocity vector fields. The POD analysis

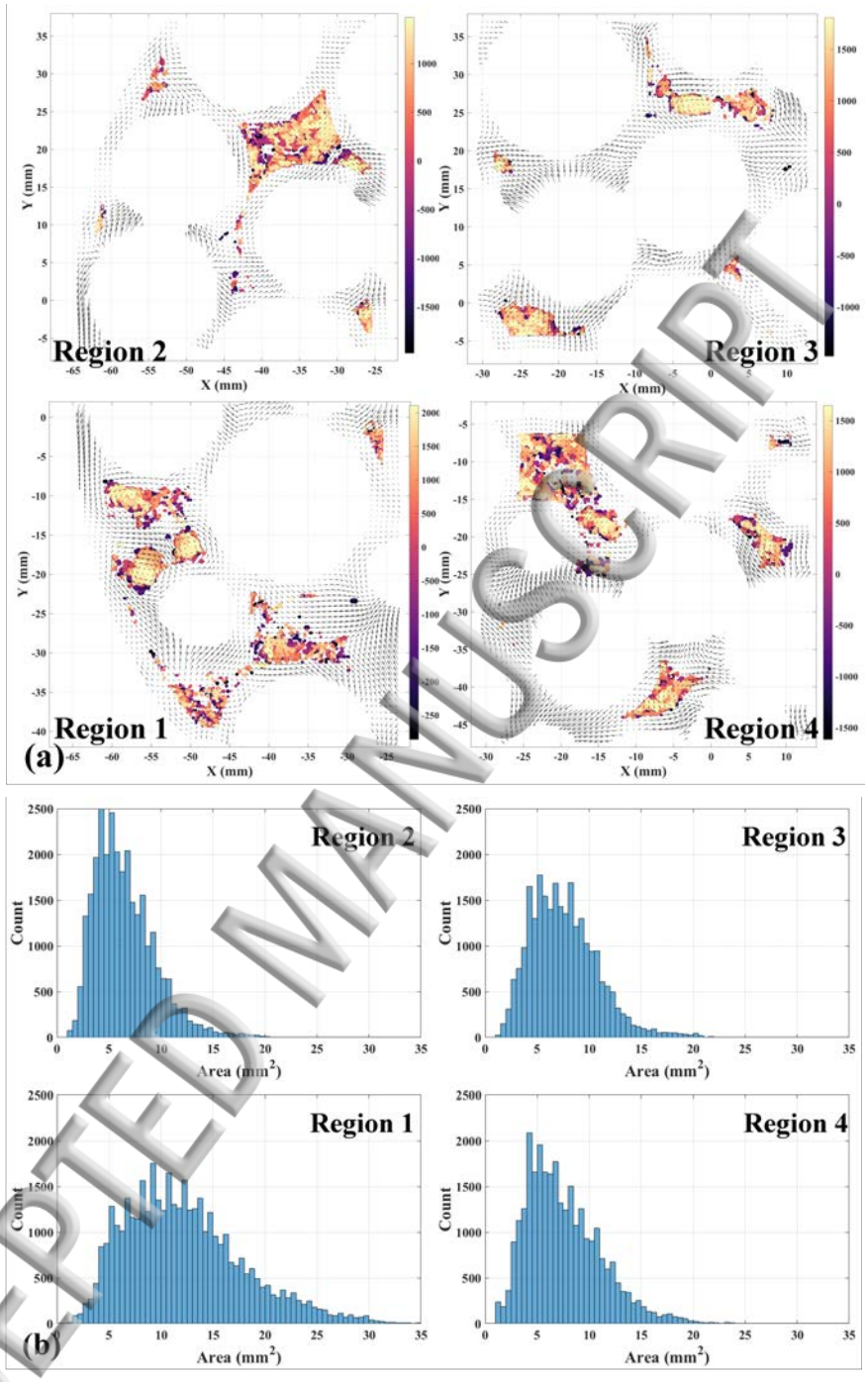

FIG. 15. *(a)* Locations, sizes, and strengths (color scale) of the identified vortices computed from the TR-PIV instantaneous velocity vector fields at Re_3 along Regions 1, 2, 3, and 4. *(b)* Histograms of the flow areas covered by the vortices identified along Regions 1, 2, 3, and 4.

was performed on the collections of instantaneous velocity snapshots. The obtained low-order POD spatial modes and POD temporal coefficients were then used to reconstruct the velocity snapshots. It should be noted that the numbers of low-order POD modes were selected for the

reconstruction to capture 99% of the total kinetic energy of the flow. Vortex identification was performed on the reconstructed velocity snapshots to extract vortex spatial distributions, circulations, areas, and populations on measurement Regions 1, 2, 3, and 4.

Figure 15 illustrates the distributions of vortices identified from the TR-PIV instantaneous velocity vector fields at Re_3, respectively, and along Regions 1, 2, 3, and 4. In these figures, the location and the size of vortices are overlaid on the mean velocity vector fields, while the color scale depicts vortex strengths. In addition, histograms were used to represent fluid areas covered by the vortices identified along each measurement region. Table IV summarizes the statistical information computed from the detected vortices on each region and for various Reynolds numbers, such as the total counts of identified vortices, N_Ω, vortex population, N_Ω/A_F (A_F is the flow area at each measurement region), normalized mean and standard deviation of vortex area, i.e., μ_A/d_p^2 and σ_A/d_p^2, and normalized mean and standard deviation of vortex strength, i.e., $\mu_\Gamma/(d_pU_m)$ and $\sigma_\Gamma/(d_pU_m)$. It should be noted that the mean and standard deviation of vortex strength were computed from the absolute strength values. It can be observed that when comparing the vortex statistics on different measurement regions for various Reynolds numbers, Region 1 had the highest number of detected vortices, which also had the greatest values of mean and standard deviation of vortex area and of vortex strength for Re_1, Re_2, and Re_3. This could be explained by the fact that Region 1 had the largest spatial gaps between neighboring spheres and the enclosure wall and the spheres, which allowed for the transportation of vortices crossing those areas. On the other hand, Regions 2, 3, and 4 had smaller spatial gaps that conformed vortices into smaller sizes, yielding lower values of the mean and standard deviation of vortex areas and strengths. For all measurements in all four regions, an increase in Reynolds number did not cause a significant change in the number of identified vortices, i.e., less than a 5% difference between the numbers of detected vortices in each region. When the Reynolds numbers increased from Re_1 to Re_3, the values of the normalized mean and standard deviation of vortex strengths at Region 1 were found to increase, while those values at Regions 2-4 were decreased. At Region 1, the mean and standard deviation of vortex area increased as the Reynolds number increased, while those values seemed to decrease for the other regions. Further investigation complemented with flow measurements of the 3D vortical structures would be essential to explain these observations. The scatter plots of the identified vortices along various measurement regions shown in Figure 15(a) confirmed our discussions in the previous section about the dependence of the density distributions and the sizes of instantaneous vortices on the local spatial gaps. There are several areas distributed in Regions 1, 2, 3, and 4, however, very few vortices were identified. A majority of vortices were found in the large gaps formed between spheres and between spheres and the enclosure wall, where the shear layers were created and evolved; or where jet/channel flows from neighboring gaps tended to merge within such areas.

The presented approach is an attempt to develop a means for characterizing the statistical characteristics of vortex distributed in various pore sizes of randomly packed beds. This approach can provide an alternative mean to evaluate the performance of high-fidelity numerical simulations, such as LES and DNS, against experimental measurements, such as PIV experiments, via compar-

ings of statistical characteristics of vortices, such as their populations, spatial distributions, and strength, that are extracted from various pore-scales. On the other hand, the obtained results could be used to construct flow parameters for modeling transports in packed beds that take into account the complex localized flow fields within pores, i.e., represented by vortex characteristics.

VII. Summary

The focus of this study is to investigate the flow mixing characteristics in a cross-flow plane and the bypass flows, i.e., flows between the enclosure wall and spheres, of randomly packed beds. TR-PIV measurements were performed on a transverse plane of a MIR facility of randomly packed spheres with an aspect ratio of 6.3 for three Reynolds numbers ranging from turbulent transition to fully turbulent flow for packed beds. The instantaneous and mean velocity fields in the transverse plane revealed swirling flow structures aligned with the axial flow. The random distribution of porosity within the packed spheres created various flow patterns including a strong bypass flow near the spheres and the enclosure wall, and a recirculation flow region formed by the interactions of the bypass flow ejecting into large spatial gaps. The peak values of u'_{rms} and v'_{rms} were found to increase approximately at the same ratio as the increase in Reynolds number. Moreover, the increase in magnitudes of the Reynolds stress profile, $u'v'$, with the increase in Reynolds numbers indicates the presence of recirculation region and shear layers between spheres. The two-point cross-correlations of the fluctuating velocities were computed and analyzed to investigate the characteristics of flow mixing in different spatial gaps between spheres and flow regions in packed beds. It was found that the increasing the Reynolds numbers from Re_1 to Re_3 did not strongly affect the estimated integral length scales, except for those in Zone 5, where ${}^{y}L_y$ decreased from 2.58 mm to 1.98 mm. The integral length scales computed for Zones 1 and 2 near the enclosure wall

TABLE IV. Statistical results of vortices identified from the TR-PIV velocity vectors on Regions 1, 2, 3 and 4 for three Reynolds numbers Re_1, Re_2 and Re_3. The values shown here are the total counts of detected vortices, N_Ω, vortex population, N_Ω/A_F (A_F is the flow area), the normalized mean and standard deviation of vortex area, i.e., μ_A/d_p^2 and σ_A/d_p^2, respectively, and the normalized mean and standard deviation of vortex strength, i.e., $\mu_\Gamma/(d_pU_m)$ and $\sigma_\Gamma/(d_pU_m)$, respectively.

	Region 1			Region 2			Region 3			Region 4		
	Re_1	Re_2	Re_3	Re_1	Re_2	Re_3	Re_1	Re_2	Re_3	Re_1	Re_2	Re_3
N_Ω	39292	38449	39834	30657	29262	29237	26820	25828	25469	29974	29450	28807
N_Ω/A_F	43.98	43.04	44.59	48.06	45.87	45.83	38.73	37.30	36.78	36.48	35.84	35.06
μ_A/d_p^2	0.021	0.022	0.025	0.015	0.013	0.013	0.017	0.016	0.015	0.016	0.015	0.015
σ_A/d_p^2	0.010	0.011	0.012	0.007	0.006	0.006	0.006	0.007	0.007	0.007	0.007	0.007
$\mu_\Gamma/(d_pU_m)$	0.349	0.372	0.401	0.309	0.267	0.248	0.335	0.313	0.292	0.260	0.250	0.240
$\sigma_\Gamma/(d_pU_m)$	0.141	0.169	0.175	0.128	0.110	0.098	0.122	0.123	0.115	0.112	0.106	0.106

were greater than those obtained for flow regions far from the wall, indicating the effects of bypass flow. The 3D vortical structures, which were reconstructed using Taylor's hypothesis, showed that the shear layers created from the small gaps of the bypass flow were stretched, then broke into smaller structures and evolved as vortex pairs when entering the larger neighboring gaps.

The POD analysis was applied to the TR-PIV velocity snapshots to extract the dominant flow structures that have important contribution to the flow mixing of packed beds. Results from the POD analysis of velocity fields in Regions 1, 2, 3, and 4 showed that the first POD modes contained 56.6%, 64.3%, 74.4%, and 64.6% of the flow total kinetic energy for Re_1, and reduced to 55.3%, 60.5%, 69.9%, and 61.3% for Re_3, respectively. The kinetic energy levels of the low-order POD modes 2, 3, and 4 were less than 3%, and the energy levels contained in the first 100 low-order POD modes at Re_3 were 87.2%, 89.2%, 91.6%, and 89.5% for Regions 1 to 4, respectively. The reduction of kinetic energy levels in the first POD modes and the slow convergence of the cumulative energy at higher Reynolds number indicated that flow mixing in the transverse plane is highly turbulent and the flow kinetic energy is widely distributed over many small-scale flow structures. Finally, a combined approach consisting of POD analysis and vortex identification to identify vortices from the TR-PIV velocity vector fields was adopted to study their characteristics, such as populations, spatial distributions, and strengths. It was found that the measurement Region 1 had the highest number of detected vortices, and the highest values of the mean and standard deviation of vortex area and strength because of its large spatial gaps, which allowed for vortex transportation in this region. Furthermore, we found that the increasing the Reynolds number did not yield significant changes in the vortex population, whereas the means and standard deviations of vortex strengths in Region 1 increased and those values at Regions 2-4 decreased. The approach presented in this study to characterize the vortex statistics within randomly packed beds could be used to access the performances of numerical simulations against experimental measurements. The obtained statistical characteristics of vortex for various pore sizes could also be used to construct flow transport models in packed beds.

VIII. Acknowledgments

This research is financially supported by the U.S. Department of Energy, NEAMS project and under a contract DE-NE0008550. The authors gratefully acknowledge Ethan Kappes and Stephen King for their support with the flow measurements.

References

[1] C. Jin, P. A. Langston, G. E. Pavlovskaya, M. R. Hall, and S. P. Rigby, "Statistics of highly heterogeneous flow fields confined to three-dimensional random porous media," Physical Review E **93**, 013122 (2016).

[2] A. Alkhalaf and E. Specht, "Prediction of cross flow mixing in the structured packed bed through cfd simulation using (fbm and pmm) and validation with experiments," Engineering Applications of Computational Fluid Mechanics **11**, 1–14 (2017).

[3] A. Boisson, P. De Anna, O. Bour, T. Le Borgne, T. Labasque, and L. Aquilina, "Reaction chain modeling of denitrification reactions during a push–pull test," Journal of Contaminant

Hydrology **148**, 1–11 (2013).

[4]L. Cueto-Felgueroso and R. Juanes, "Nonlocal interface dynamics and pattern formation in gravity-driven unsaturated flow through porous media," Physical Review Letters **101**, 244504 (2008).

[5]G. Chiogna, O. A. Cirpka, P. Grathwohl, and M. Rolle, "Transverse mixing of conservative and reactive tracers in porous media: Quantification through the concepts of flux-related and critical dilution indices," Water Resources Research **47** (2011).

[6]D. A. Nield, A. Bejan, *et al.*, *Convection in porous media*, Vol. 3 (Springer, 2006).

[7]F. A. Dullien, *Porous media: fluid transport and pore structure* (Academic press, 2012).

[8]U. Scheven, "Pore-scale mixing and transverse dispersivity of randomly packed monodisperse spheres," Physical Review Letters **110**, 214504 (2013).

[9]D. Hlushkou, S. Piatrusha, and U. Tallarek, "Impact of diffusion on transverse dispersion in two-dimensional ordered and random porous media," Physical Review E **95**, 063108 (2017).

[10]C.-Y. Wang, "Fundamental models for fuel cell engineering," Chemical reviews **104**, 4727–4766 (2004).

[11]A.-R. Khaled and K. Vafai, "The role of porous media in modeling flow and heat transfer in biological tissues," International Journal of Heat and Mass Transfer **46**, 4989–5003 (2003).

[12]A. E. Scheidegger, "The physics of flow through porous media," Tech. Rep. (University of Toronto Press, Toronto, 1974).

[13]M. Sahimi, *Flow and transport in porous media and fractured rock: from classical methods to modern approaches* (John Wiley & Sons, 2011).

[14]J. Bear, *Dynamics of fluids in porous media* (Courier Corporation, 2013).

[15]P. de Anna, B. Quaife, G. Biros, and R. Juanes, "Prediction of the low-velocity distribution from the pore structure in simple porous media," Physical Review Fluids **2**, 124103 (2017).

[16]P. De Anna, T. Le Borgne, M. Dentz, A. M. Tartakovsky, D. Bolster, and P. Davy, "Flow intermittency, dispersion, and correlated continuous time random walks in porous media," Physical Review Letters **110**, 184502 (2013).

[17]P. d. Anna, J. Jimenez-Martinez, H. Tabuteau, R. Turuban, T. Le Borgne, M. Derrien, and Y. Meheust, "Mixing and reaction kinetics in porous media: An experimental pore scale quantification," Environmental Science & Technology **48**, 508–516 (2013).

[18]S. Ergun, "Fluid flow through packed columns," Chem. Eng. Prog. **48**, 89–94 (1952).

[19]G. des Kerntechnischen Ausschusses, "Kta 3102.3, reactor core design of high-temperature gas-cooled reactors part 3: loss of pressure through friction in pebble bed cores," Tech. Rep. (Berlin, Germany: Nuclear Safety Standards Commission, 1981).

[20]K. Wirth, "Pressure drop in fixed beds," VDI Heat Atlas , 1106–1110 (2010).

[21]A. Dixon and D. Cresswell, "Effective heat transfer parameters for transient packed-bed models," AIChE journal **32**, 809–819 (1986).

[22]D. Gunn, "Axial and radial dispersion in fixed beds," Chemical Engineering Science **42**, 363–373 (1987).

[23]C.-Y. Wen, L.-t. Fan, *et al.*, *Models for flow systems and chemical reactors* (M. Dekker, 1975).

[24]M. J. de Lemos and M. H. Pedras, "Recent mathematical models for turbulent flow in saturated rigid porous media," Journal of Fluids Engineering **123**, 935–940 (2001).

[25]B. Antohe and J. Lage, "A general two-equation macroscopic turbulence model for incompressible flow in porous media," International Journal of Heat and Mass Transfer **40**, 3013–3024 (1997).

[26]D. Getachew, W. Minkowycz, and J. Lage, "A modified form of the κ–ε model for turbulent flows of an incompressible fluid in porous media," International Journal of Heat and Mass Transfer **43**, 2909–2915 (2000).

[27]T. Masuoka and Y. Takatsu, "Turbulence model for flow through porous media," International Journal of Heat and Mass Transfer **39**, 2803–2809 (1996).

[28]A. Nakayama and F. Kuwahara, "A macroscopic turbulence model for flow in a porous medium," Journal of fluids engineering **121**, 427–433 (1999).

[29]B. Wood, S. Apte, J. Liburdy, R. Ziazi, X. He, J. Finn, and V. Patil, "A comparison of measured and modeled velocity fields for a laminar flow in a porous medium," Advances in Water Resources **85**, 45–63 (2015).

[30]Y. A. Hassan, "Large eddy simulation in pebble bed gas cooled core reactors," Nuclear Engineering and Design **238**, 530–537 (2008).

[31]A. Shams, F. Roelofs, E. Komen, and E. Baglietto, "Quasi-direct numerical simulation of a pebble bed configuration. part i: Flow (velocity) field analysis," Nuclear Engineering and Design **263**, 473–489 (2013).

[32]A. Shams, F. Roelofs, E. Komen, and E. Baglietto, "Quasi-direct numerical simulation of a pebble bed configuration, part-ii: Temperature field analysis," Nuclear Engineering and Design **263**, 490–499 (2013).

[33]L. Fick, E. Merzari, and Y. Hassan, "Direct numerical simulation of the flow through a structured pebble bed near a wall boundary," in *ASME/JSME/KSME 2015 Joint Fluids Engineering Conference* (American Society of Mechanical Engineers, 2015) pp. V001T03A008–V001T03A008.

[34]L. H. Fick, E. Merzari, O. Marin, and Y. A. Hassan, "Investigation of the dynamics of incompressible flow in domains of multiple close-packed spheres," in *ASME 2017 Fluids Engineering Division Summer Meeting* (American Society of Mechanical Engineers, 2017) pp. V01BT12A007–V01BT12A007.

[35]L. H. Fick, E. Merzari, and Y. A. Hassan, "Direct numerical simulation of pebble bed flows: database development and investigation of low-frequency temporal instabilities," Journal of Fluids Engineering **139**, 051301 (2017).

[36]W. Johnston, A. Dybbs, and R. Edwards, "Measurement of fluid velocity inside porous media with a laser anemometer," Physics of Fluids **18**, 913–914 (1975).

[37]A. Yarlagadda and A. Yoganathan, "Experimental studies of model porous media fluid dynamics," Experiments in Fluids **8**, 59–71 (1989).

[38]S. Haam, R. Brodkey, I. Fort, L. Klaboch, M. Placnik, and V. Vanecek, "Laser Doppler anemometry measurements in an index of refraction matched column in the presence of dispersed beads: part i," International Journal of Multiphase Flow **26**, 1401–1418 (2000).

[39]J. Stephenson and W. Stewart, "Optical measurements of porosity and fluid motion in packed beds," Chemical Engineering Science **41**, 2161–2170 (1986).

[40]L. M. Peurrung, M. Rashidi, and T. J. Kulp, "Measurement of porous medium velocity fields and their volumetric averaging characteristics using particle tracking velocimetry," Chemical Engineering Science **50**, 2243–2253 (1995).

[41]M. Moroni and J. H. Cushman, "Statistical mechanics with three-dimensional particle tracking velocimetry experiments in the study of anomalous dispersion. ii. experiments," Physics of Fluids **13**, 81–91 (2001).

[42]A. Y. Huang, M. Y. Huang, H. Capart, and R.-H. Chen, "Optical measurements of pore geometry and fluid velocity in a bed of irregularly packed spheres," Experiments in Fluids **45**, 309–321 (2008).

[43]S. Saleh, J. Thovert, and P. Adler, "Measurement of two-dimensional velocity fields in porous media by particle image displacement velocimetry," Experiments in Fluids **12**, 210–212 (1992).

[44]M. A. Northrup, T. J. Kulp, S. M. Angel, and G. F. Pinder, "Direct measurement of interstitial velocity field variations in a porous medium using fluorescent-particle image velocimetry," Chemical Engineering Science **48**, 13–21 (1993).

[45]Y. A. Hassan and E. Dominguez-Ontiveros, "Flow visualization in a pebble bed reactor experiment using PIV and refractive index matching techniques," Nuclear Engineering and Design **238**, 3080–3085 (2008).

[46]V. A. Patil and J. A. Liburdy, "Optical measurement uncertainties due to refractive index mismatch for flow in porous media," Experiments in Fluids **53**, 1453–1468 (2012).

[47]V. A. Patil and J. A. Liburdy, "Flow characterization using piv measurements in a low aspect ratio randomly packed porous bed," Experiments in Fluids **54**, 1497 (2013).

[48]V. A. Patil and J. A. Liburdy, "Turbulent flow characteristics in a randomly packed porous bed based on particle image velocimetry measurements," Physics of Fluids **25**, 043304 (2013).

[49]S. Khayamyan, T. S. Lundström, J. G. I. Hellström, P. Gren, and H. Lycksam, "Measurements of transitional and turbulent flow in a randomly packed bed of spheres with particle image velocimetry," Transport in Porous Media **116**, 413–431 (2017).

[50]T. Nguyen, E. Kappes, S. King, Y. Hassan, and V. Ugaz, "Time-resolved PIV measurements in a low-aspect ratio facility of randomly packed spheres and flow analysis using modal decomposition," Experiments in Fluids **59**, 127 (2018).

[51]S. Khayamyan, T. S. Lundström, P. Gren, H. Lycksam, and J. G. I. Hellström, "Transitional and turbulent flow in a bed of spheres as measured with stereoscopic particle image velocimetry," Transport in Porous Media **117**, 45–67 (2017).

[52]T. Nguyen, E. Kappes, S. King, Y. Hassan, and V. Ugaz, "Spatiotemporally resolved PIV/SPIV velocity measurements in a MRI facility of randomly packed spheres," in *InterPore 10th Annual*

Meeting and Jubilee (International Society for Porous Media, 2018).
[53]J. Goodling, R. Vachon, W. Stelpflug, S. Ying, and M. Khader, "Radial porosity distribution in cylindrical beds packed with spheres," Powder Technology **35**, 23–29 (1983).
[54]H. Sato, R. Johnson, and R. Schultz, "Computational fluid dynamic analysis of core bypass flow phenomena in a prismatic vhtr," Annals of Nuclear Energy **37**, 1172–1185 (2010).
[55]S.-J. Yoon, C.-Y. Jin, M.-H. Kim, and G.-C. Park, "Experimental and computational assessment of core bypass flow in block-type very high temperature reactor," Nuclear Technology **175**, 419–434 (2011).
[56]R. W. Johnson and H. Sato, "Bypass flow computations using a one-twelfth symmetric sector for normal operation in a 350 mwth prismatic vhtr," Nuclear Engineering and Design **251**, 84–91 (2012).
[57]N. Amini and Y. A. Hassan, "An investigation of matched index of refraction technique and its application in optical measurements of fluid flow," Experiments in Fluids **53**, 2011–2020 (2012).
[58]M. Raffel, C. E. Willert, S. Wereley, and J. Kompenhans, *Particle image velocimetry: a practical guide* (Springer, 2013).
[59]C. Fort, C. D. Fu, N. A. Weichselbaum, and P. M. Bardet, "Refractive index and solubility control of para-cymene solutions for index-matched fluid–structure interaction studies," Experiments in Fluids **56**, 210 (2015).
[60]T. Nguyen, N. Goth, P. Jones, S. Lee, R. Vaghetto, and Y. Hassan, "PIV measurements of turbulent flows in a 61-pin wire-wrapped hexagonal fuel bundle," International Journal of Heat and Fluid Flow **65**, 47–59 (2017).
[61]T. Nguyen, N. Goth, P. Jones, R. Vaghetto, and Y. Hassan, "Stereoscopic PIV measurements of near-wall flow in a tightly packed rod bundle with wire spacers," Experimental Thermal and Fluid Science **92**, 420–435 (2018).
[62]R. J. Adrian, "Particle-imaging techniques for experimental fluid mechanics," Annual Review of Fluid Mechanics **23**, 261–304 (1991).
[63]A. Eckstein and P. P. Vlachos, "Digital particle image velocimetry (DPIV) robust phase correlation," Measurement Science and Technology **20**, 055401 (2009).
[64]A. Eckstein and P. P. Vlachos, "Assessment of advanced windowing techniques for digital particle image velocimetry (DPIV)," Measurement Science and Technology **20**, 075402 (2009).
[65]A. C. Eckstein, J. Charonko, and P. Vlachos, "Phase correlation processing for DPIV measurements," Experiments in Fluids **45**, 485–500 (2008).
[66]T. Guo, M. J. Rau, P. P. Vlachos, and S. V. Garimella, "Axisymmetric wall jet development in confined jet impingement," Physics of Fluids **29**, 025102 (2017).
[67]J. Westerweel, "Efficient detection of spurious vectors in particle image velocimetry data," Experiments in Fluids **16**, 236–247 (1994).
[68]B. H. Timmins, B. W. Wilson, B. L. Smith, and P. P. Vlachos, "A method for automatic estimation of instantaneous local uncertainty in particle image velocimetry measurements," Experiments in Fluids **53**, 1133–1147 (2012).

[69]B. M. Wilson and B. L. Smith, "Uncertainty on PIV mean and fluctuating velocity due to bias and random errors," Measurement Science and Technology **24**, 035302 (2013).

[70]J. J. Charonko and P. P. Vlachos, "Estimation of uncertainty bounds for individual particle image velocimetry measurements from cross-correlation peak ratio," Measurement Science and Technology **24**, 065301 (2013).

[71]A. Boomsma, S. Bhattacharya, D. Troolin, S. Pothos, and P. Vlachos, "A comparative experimental evaluation of uncertainty estimation methods for two-component PIV," Measurement Science and Technology **27**, 094006 (2016).

[72]A. Sciacchitano and B. Wieneke, "Piv uncertainty propagation," Measurement Science and Technology **27**, 084006 (2016).

[73]A. Sciacchitano, D. R. Neal, B. L. Smith, S. O. Warner, P. P. Vlachos, B. Wieneke, and F. Scarano, "Collaborative framework for PIV uncertainty quantification: comparative assessment of methods," Measurement Science and Technology **26**, 074004 (2015).

[74]D. R. Neal, A. Sciacchitano, B. L. Smith, and F. Scarano, "Collaborative framework for PIV uncertainty quantification: the experimental database," Measurement Science and Technology **26**, 074003 (2015).

[75]G. I. Taylor, "The spectrum of turbulence," in *Proceedings of the Royal Society of London A: Mathematical, Physical and Engineering Sciences*, Vol. 164 (The Royal Society, 1938) pp. 476–490.

[76]T. Matsuda and J. Sakakibara, "On the vortical structure in a round jet," Physics of Fluids **17**, 025106 (2005).

[77]C. Van Doorne and J. Westerweel, "Measurement of laminar, transitional and turbulent pipe flow using stereoscopic-PIV," Experiments in Fluids **42**, 259–279 (2007).

[78]B. Ganapathisubramani, K. Lakshminarasimhan, and N. Clemens, "Investigation of three-dimensional structure of fine scales in a turbulent jet by using cinematographic stereoscopic particle image velocimetry," Journal of Fluid Mechanics **598**, 141–175 (2008).

[79]F. Diez, M. Torregrosa, and S. Pothos, "A comparison between round turbulent jets and particle-laden jets in crossflow by using time-resolved stereoscopic particle image velocimetry," Journal of Fluids Engineering **133**, 091301 (2011).

[80]D. Garcia, "Robust smoothing of gridded data in one and higher dimensions with missing values," Computational Statistics & Data Analysis **54**, 1167–1178 (2010).

[81]D. Garcia, "A fast all-in-one method for automated post-processing of PIV data," Experiments in Fluids **50**, 1247–1259 (2011).

[82]P. R. Spalart, "Contributions of numerical simulation data bases to the physics, modeling, and measurement of turbulence," Advances In Turbulence , 11 (1988).

[83]G. P. Romano, "Analysis of two-point velocity measurements in near-wall flows," Experiments in Fluids **20**, 68–83 (1995).

[84]T. Nguyen and Y. Hassan, "Stereoscopic particle image velocimetry measurements of flow in a rod bundle with a spacer grid and mixing vanes at a low reynolds number," International Journal

of Heat and Fluid Flow **67**, 202–219 (2017).

[85]F. Kerhervé and J. Fitzpatrick, "Measurement and analysis of the turbulent length scales in jet flows," Experiments in Fluids **50**, 637–651 (2011).

[86]M. Falchi and G. P. Romano, "Evaluation of the performance of high-speed piv compared to standard piv in a turbulent jet," Experiments in Fluids **47**, 509–526 (2009).

[87]J. L. Lumley, "The structure of inhomogeneous turbulent flows," Atmospheric Turbulence and Radio Wave Propagation , 166–178 (1967).

[88]G. Berkooz, P. Holmes, and J. L. Lumley, "The proper orthogonal decomposition in the analysis of turbulent flows," Annual Review of Fluid Mechanics **25**, 539–575 (1993).

[89]P. Holmes, J. L. Lumley, and G. Berkooz, *Turbulence, coherent structures, dynamical systems and symmetry* (Cambridge University Press, 1998).

[90]L. Sirovich and M. Kirby, "Low-dimensional procedure for the characterization of human faces," Journal of The Optical Society of America **4**, 519–524 (1987).

[91]Z.-S. She, E. Jackson, and S. A. Orszag, "Intermittent vortex structures in homogeneous isotropic turbulence," Nature **344**, 226 (1990).

[92]J. C. Hunt, A. A. Wray, and P. Moin, "Eddies, streams, and convergence zones in turbulent flows," in *Proceedings of the 1988 Summer Program of the Center for Turbulence Research (NASA Ames/Stanford University, 1988)* (1988).

[93]M. S. Chong, A. E. Perry, and B. J. Cantwell, "A general classification of three-dimensional flow fields," Physics of Fluids A: Fluid Dynamics **2**, 765–777 (1990).

[94]J. Zhou, R. J. Adrian, S. Balachandar, and T. Kendall, "Mechanisms for generating coherent packets of hairpin vortices in channel flow," Journal of Fluid Mechanics **387**, 353–396 (1999).

[95]J. Jeong and F. Hussain, "On the identification of a vortex," Journal of Fluid Mechanics **285**, 69–94 (1995).

[96]Q. Chen, Q. Zhong, M. Qi, and X. Wang, "Comparison of vortex identification criteria for planar velocity fields in wall turbulence," Physics of Fluids **27**, 085101 (2015).

[97]R. Adrian, K. Christensen, and Z.-C. Liu, "Analysis and interpretation of instantaneous turbulent velocity fields," Experiments in fluids **29**, 275–290 (2000).

[98]J. Carlier and M. Stanislas, "Experimental study of eddy structures in a turbulent boundary layer using particle image velocimetry," Journal of Fluid Mechanics **535**, 143–188 (2005).

[99]V. Kolář, "Vortex identification: New requirements and limitations," International Journal of Heat and Fluid Flow **28**, 638–652 (2007).

[100]Y. Maciel, M. Robitaille, and S. Rahgozar, "A method for characterizing cross-sections of vortices in turbulent flows," International Journal of Heat and Fluid Flow **37**, 177–188 (2012).

[101]L. Graftieaux, M. Michard, and N. Grosjean, "Combining piv, pod and vortex identification algorithms for the study of unsteady turbulent swirling flows," Measurement Science and Technology **12**, 1422 (2001).